DOI:
10.1126/sciimmunol.aau6598

Document Version
Peer reviewed version

Intrinsic properties of human germinal-center B cells set antigen-affinity thresholds

Kihyuck Kwak[1], Nicolas Quizon[1], Haewon Sohn[1], Avva Saniee[1], Javier Manzella-Lapeira[1], Prasida Holla[1], Joseph Brzostowski[1], Jinghua Lu[1], HengYi Xie[2], Chenguang Xu[2], Katelyn M. Spillane[3], Pavel Tolar[4,5] and Susan K. Pierce[1*]

[1]Laboratory of Immunogenetics, National Institute of Allergy and Infectious Diseases, National Institutes of Health, Rockville, Maryland 20852, USA.

[2]MOE Key Laboratory of Protein Sciences, Collaborative Innovation Center for Diagnosis and Treatment of Infectious Diseases, School of Life Sciences, Institute for Immunology, Tsinghua University, Beijing, China.

[3]Department of Physics, King's College London, London WC2R 2LS, UK.

[4]Immune Receptor Activation Laboratory, The Francis Crick Institute, London NW1 1AT, England, UK.

[5]Division of Immunology and Inflammation, Imperial College London, London SW7 2AZ, England, UK.

[*]To whom correspondence should be addressed:

Susan K. Pierce

5625 Fishers Lane, Room 4S04

Rockville, MD 20852 USA

E-mail: *spierce@nih.gov*

Phone: (301) 496-9589; Fax: (301) 594-9990

Abstract

Protective antibody responses to vaccination or infection depend on affinity maturation, a process by which high-affinity germinal center (GC) B cells are selected based on their ability to bind, gather and present antigen to T follicular helper (Tfh) cells. Here we show that human GC B cells have intrinsically higher affinity thresholds for both B cell antigen receptor (BCR) signaling and antigen gathering as compared to naïve B cells and that these functions are mediated by distinct cellular structures and pathways that ultimately lead to antigen-affinity- and Tfh cell-dependent differentiation to plasma cells. GC B cells bound antigen through highly dynamic, actin- and ezrin-rich pod-like structures that concentrated BCRs. The behavior of these structure was dictated by the intrinsic antigen-affinity thresholds of GC B cells. Low affinity antigens triggered continuous engagement and dis-engagement of membrane associated antigens whereas high affinity antigens induced stable synapse formation. The pod-like structures also mediated affinity-dependent antigen internalization by unconventional pathways distinct from those of naïve B cells. Thus, intrinsic properties of human GC B cells set thresholds for affinity selection.

Introduction

A hallmark of immunological memory is the affinity maturation of antibody responses (*1, 2*). Underlying affinity maturation is the accumulation of mutations in the IgVH and IgVL complementary determining regions of antibodies through a stochastic process of somatic hypermutation (SHM) and the subsequent competitive selection of B cells that have acquired affinity-enhancing mutations for the immunizing antigen or invading pathogen (*2-5*). Indeed, the development of vaccines for diseases for which we currently have none, including HIV-AIDS, will benefit from an understanding of the cellular and molecular mechanisms underlying antigen selection and affinity maturation in human B cells.

The processes of SHM and affinity-based selection occur in spatially-distinct, specialized microenvironments within B cell follicles of secondary lymphoid organs termed germinal center (GC) dark zones (DZ) and light zones (LZ), respectively (*5-7*). Our understanding of the details of the events that precede GC formation and are required for selection of high-affinity antigen-specific B cells within GC light zones has expanded remarkably over the last few years, almost exclusively from studies in mouse models. We now understand that naïve B cells first encounter antigens on the surfaces of subcapsular sinus macrophages, dendritic cells (DC), or follicular dendritic cells (FDC) (*8, 9*). B cell engagement of the cell-surface associated antigen triggers BCR signaling and antigen extraction, internalization, processing and presentation of the antigen on MHC class II molecules (*4, 10*). B cells then migrate to the border of the follicles with the T cell zone where they present antigen to T cells that have been recently primed by antigen presented on DCs to differentiate into T follicular helper (Tfh) cells (*11, 12*). The resulting B cell-Tfh cell interaction drives B cell proliferation and differentiation into effector cells including short-lived plasma cells (PCs), GC-independent memory B cells (MBCs) and GC cells (*13-16*).

GC B cells first enter GC DZs where they proliferate and undergo SHM prior to entering the GC LZs where antigen-affinity based selection occurs (*17-19*). Current evidence indicates that selection is a competitive process dependent in large part on the amount of antigen B cells are able to gather, process and present to Tfh cells (*20*). LZ GC B cells have several potential fates that depend on their interactions with Tfh cells including, apoptosis, positive selections for re-entry into the DZ for further proliferative expansion and SHM or differentiation into MBCs or long-lived PCs. MBCs have been shown to have fewer SHMs and to be of lower affinity as compared to PCs (*21*) and Shinnakasu *et al.* (*22*) recently provided evidence that in mice MBCs differentiate from low-affinity LZ GC B cells as a result of weak help from Tfh cells. In contrast, Krautler *et al.* (*23*) showed in mice that differentiation into PCs is induced among a discrete subset of high-affinity LZ GC B cells initiated by the engagement of antigen and completed by Tfh cells.

Thus, there appear to be at least two key checkpoints in the process of affinity maturation, one for naïve B cells and one for LZ GC B cells. At these checkpoints, the affinity of B cell for its antigen is tested by the ability of the BCR to differentially signal in response to and internalize, process and present antigen to T cells. From studies primarily carried out using naïve mouse B cells we understand that B cells form immune synapses upon engagement of membrane bound antigen from which BCRs both signal and extract antigen from the membrane and internalize it for processing and presentation (*24*). Affinity discrimination is achieved in part through mechanical forces that the B cell exerts on the BCR-antigen complex, rupturing most BCR-antigen bonds and promoting internalization and presentation of high-affinity BCRs (*25*). Recent studies provided evidence that mouse GC B cells exert stronger pulling forces on the BCR as compared to naïve B cells resulting in better affinity discrimination (*26*). However,

despite the central role of these checkpoints in affinity selection and maturation we have a limited understanding of the potential of human naïve or GC B cells at these checkpoints to discriminate antigen affinity or of the cellular or molecular mechanisms that facilitate affinity discrimination by naïve and GC B cells. Here we show that as compared to human naïve B cells, GC B cells have a higher affinity threshold for antigen binding, gathering and internalization. We describe the novel structures through which GC B cell engage antigen and the pathways by which GC B cells internalize antigen. These findings provide a mechanistic framework for antigen affinity discrimination by human GC B cells.

Results

GC B Cells Engage Antigen through BCRs Concentrated in Novel F-Actin and Ezrin-Rich Pod-like Structures

To understand how human naïve and GC B cells engage membrane-associated antigens, we obtained differential interference contrast (DIC) and interference reflection microscopy (IRM) images of live B cells isolated from human tonsils and placed on antigen-containing membranes (Fig. 1A and Movie S1). B cell sub-populations were purified from single cell suspensions of human tonsils B cells obtained by negative selection and sorted based on expression of CD10, IgD and CXCR4 into the four B cell subpopulations (fig. S1); naïve B cells (IgD^+ $CD10^-$); MBCs (IgD^- $CD10^-$); LZ GC B cells (IgD^- $CD10^+$ $CXCR4^{Lo}$) and DZ GC B cells (IgD^- $CD10^+$ $CXCR4^{Hi}$). To further characterize these purified subpopulations we quantified the cell surface expression of the BCR by flow cytometry using fluorescently conjugated antibodies specific for either the λ or κ light chains. Naïve B cells expressed the highest level of BCR followed by MBCs, LZ GC and DZ GC B cells (fig. S2A). The expression of IgM, IgG, IgA

isotypes was also lower on GC B cells (fig. S2B). As a surrogate membrane-associated antigen we used streptavidin-conjugated $F(ab')_2$ light chain-specific antibodies (anti-λ/κ) attached to biotinylated lipids incorporated into fluid planar lipid bilayers (PLBs). Naïve and LZ GC B cells were placed on antigen-containing PLBs and DIC and IRM images were obtained. DIC provided images of unstained live B cells. IRM uses polarized light to form images of the B cells on the PLBs in which the intensity of the signal is a measure of the proximity of the cell's membrane to the PLB. Naïve B cells appeared to form large flat, stable contact areas with the antigen-containing PLB and maintain active ruffling around the cell's periphery consistent with conventional immune synapses (Fig. 1A and Movie S1). The stable interaction on the naïve B cell with the bilayer over time was quantified and shown as a kymograph (Fig. 1B). The behavior of the LZ GC B cells on the antigen bilayer was remarkably different. Rather than forming flat stable contact areas, the cells touched the bilayer through highly dynamic, large pod-like structures (Fig. 1A and Movie S1). This behavior is displayed as a kymograph showing the dynamic movement of the cell over time (Fig. 1B). The LZ GC pod-like structures appeared to form in response to antigen as in the absence of antigen, the LZ GC B cell surfaces were smooth and the cells made contact with the bilayer through a small, stable area as evident in the IRM images (Fig. 1A and Movie S1). We extended the IRM analyses to include a comparison of DZ GCs in addition to naïve and LZ GC B cells. Naïve B cells rapidly responded to the antigen-containing PLB forming flat contact areas in uniform close proximity to the membrane that were stable over 20 min (Fig. 1C and Movie S2). In contrast, both DZ and LZ GC B cells made small, transient, highly dynamic contacts with the antigen-containing PLB for several minutes before the contacts stabilized but never reached the same high-intensity, uniform contact areas observed for naïve B cells. Quantification of the IRM images by several methods, including the intensity

of the image from the center of the contact area to the edge (fig. S2C), the percent change in intensity from frame to frame (fig. S2D) and the number of contact sites over time (fig. S2E), supported the conclusion that naïve B cells rapidly formed uniform contact with the antigen-containing PLB in contrast to GC B cells that contacted the PLB in highly dynamic small points over several minutes.

To determine a role of actin in antigen-contact, we used super resolution stimulated emission depletion (STED) microscopy to obtain nanoscale images of the organization of F-actin in naïve and LZ GC B cells placed on antigen-containing PLBs for 25 min, fixed, permeabilized and stained with Alexa Fluor 488-conjugated phalloidin (Fig. 1D). The high-resolution images showed that naïve B cells formed conventional mesh-like F-actin structures in the contact area with weak actin signal intensity. In contrast, LZ GC B cells showed a high intensity punctate pattern of F-actin-rich structures primarily in the cell's periphery. We used confocal microscopy to determine the degree of colocalization of the BCR and F-actin in the area of contact. For naïve B cells, both the BCR and F-actin were spread over the contact area with little correlation between the variation in intensities of the BCRs and F-actin across the cell suggesting that the BCR clusters were not directly associated with polymerized F-actin (Fig. 1E). In contrast, in LZ GC B cells the BCR showed a punctate pattern of intensity and peaks of BCR intensity were associated with peaks of F-actin intensity that occurred predominantly in the B cell's periphery (Fig. 1E) suggesting that the BCRs were associated with actin-rich structures.

We also determined the amount of ezrin concentrated in the contact area of the B cells with the antigen-containing PLB and the degree of colocalization of ezrin with F-actin by confocal microscopy. Ezrin is a cytoplasmic peripheral membrane protein that is enriched in actin-rich cell surface projections (*27-29*) and regulates morphological and cytoskeletal changes

in B cells (*30*). By flow cytometry ezrin expression in GC B cells was approximately 10 fold higher as compared to naïve B cells (fig. S2F). In naïve B cells ezrin was primarily in the cell periphery where ezrin and F-actin were only partially colocalized (Fig. 1F). In contrast in LZ GC B cells ezrin was concentrated in a punctate pattern and was more highly colocalized with F-actin (Fig. 1F) suggesting that the GC B cell pod-like structures were both actin- and ezrin-rich.

Confocal Z-stack 3D images of cross sections of naïve and LZ GC B cells placed on antigen-containing PLBs revealed remarkable details of cellular architecture in the contact area that was consistent with the DIC, IRM, STED and confocal images (Fig. 1G). Naïve B cells formed contact with the antigen-containing PLB in a single plane in close opposition to the PLB resulting in a relatively uniform distribution of BCRs under a plane of F-actin. In contrast, LZ GC B cells contacted the antigen-containing PLB through actin-rich pod-like structures the tips of which concentrated BCRs. The dimensions of these structures were approximately 0.2-0.5um in diameter by 1.5um in length, much larger than microvilli through which T cells have been recently demonstrated to search for antigen (*31*). These structures were also evident by scanning electron microscopy (SEM) (Fig. 1H). By SEM, in the resting state, LZ GC B cells and naïve B cells showed distinct morphologies with LZ GC B cells having a corrugated membrane topology with long, thin protrusions, whereas naïve B cells had smoother membranes with short, thick bulges. More pronounced differences were observed between naïve B cells and LZ GC B cells that were activated on antigen-coated PLBs. Naïve B cells showed a flat area of contact with the bilayer visible in SEM in both top and side views in contrast to LZ GC cells in which pod-like contacts were visible in the side view.

The observation that BCRs were concentrated in the area of contact of the pod-like structures with the antigen-containing PLB predicted that antigen gathered from the PLB would

also be concentrated in the contact areas of the pod-like structures. LZ GC B cells were placed on PLB containing fluorescently-labeled anti-λ/κ for 20 min and imaged. The DIC and antigen merged image clearly showed antigen concentrated at the ends of the pod-like structures (Fig. 1I).

Human GC B Cells Signal in Response to and Exert Pulling Forces on Membrane Bound Antigens through Pod-like Structures

To define the spatial distribution of antigen-activated BCRs on naïve B cells and GC B cells, we characterized the recruitment of components of the BCR signaling cascade to the BCRs in the contact areas between the B cells and the antigen-containing PLBs. BCRs were labeled with Alexa Fluor 488- or Alexa Fluor 647-Fab anti-IgM for naïve B cells or Alexa Fluor 488- or Alexa Fluor 647-Fab anti-IgG for GC B cells and B cells were placed on antigen-containing PLBs for 7 or 25 min. Cells were fixed, permeabilized and stained with fluorescently conjugated antibodies specific for the phosphorylated forms of kinases and phosphatases activated by the initiation of BCR signaling including PI3K and SHP-1 (Fig. 2A) and Syk, PLCγ2, Btk, Vav and Cbl (fig. S3A and S3B). Naïve B cells spread on the antigen-containing PLB over 25 min and pPI3K and pSHP-1 accumulated with BCRs in the contact area, forming a central cSMAC structure (Fig. 2A). In contrast, GC B cells did not form centralized BCR-pPI3K and -pSHP-1 clusters but rather pPI3K and pSHP-1 were concentrated with BCRs in a punctate pattern primarily in the cell periphery consistent with BCRs signaling through pod-like structures. Quantification of images showed that pPI3K and pSHP-1 were recruited earlier to naïve BCRs as compared to GC B cells but were more highly colocalized with the BCRs in GC B cells as compared to naïve B cells both in resting cells and at early and late phases of the response (Fig.

2B). Similarly, the colocalization of pSyk, pPLCγ2, pVav, pBtk, pCbl and CD19 with the BCR was consistently higher in GC cells as compared to naïve B cells (fig. S3B, S3C and Movie S3) but similar between IgM and IgG GC B cells (fig. S3D). Time-lapse live cell TIRFM imaging of the growth of individual BCR microclusters showed that microclusters grew rapidly on naïve B cells whereas growth of GC B cell BCR microclusters was slower (fig. S3E). Taken together these finding indicate that GC B cells signal through pod-like structures and that the formation of GC B cell BCR microclusters is slower as compared to naïve but these signaling active clusters may be more stable.

We also compared the ability of LZ and DZ GC B cells and naïve B cells to exert a pulling force on membrane antigen. To do so we used F(ab')2 anti-κ/λ as a surrogate antigen conjugated to a 9 pN DNA-based force sensor attached to PLBs (fig. S4A). The force sensor contained a central DNA hairpin that unwinds when pulling forces are exerted by the BCR on the antigen, displacing an Atto 647N dye from a dark quencher at the base of the hairpin resulting in increased Atto 647N fluorescence over the fluorescence of a force insensitive dye Atto 550 attached to the double stranded DNA at the top of the sensor. Opening is expressed as the ratio of the signal intensity of Atto 647N to that of Atto 550. Control sensors lack the hairpin and cannot be opened by force.

Time-lapse TIRFM imaging of the sensor's Atto 550 fluorescence showed that naïve B cells rapidly spread over the PLB capturing the sensor and accumulating it in the center of the contact area within 3 to 4 min, forming a flat immune synapse where the sensor persisted for several min (Fig. 2C and Movie S4). Over this time, we detected only rare appearances of Atto 647N fluorescence indicating that naïve B cells were not exerting at least a 9 pN force on the antigen. Imaging the Atto 550 intensity of the antigen-containing sensor for LZ GC B cells

showed a punctate pattern of clustered intensity consistent with the sensor binding to BCR concentrated in the pod-like structures. We observed robust Atto 647N intensity that coincided with areas of Atto 550 intensity (Fig. 2C), indicating that LZ GC B cells were able to exert a pulling force on the antigen of at least 9 pN through the pod-like structures. Analysis of DZ GC B cells showed a similar result. Quantification of the sensor opening showed that human naïve B cells were unable to exert a force sufficient to open the sensor (Fig. 2D and Movie S4). In contrast, both LZ and DZ GC B cells were able to exert at least a 9 pN force on the antigen.

To confirm that the LZ GC B cell's pulling force was exerted by the BCRs in the actin-rich pod-like structures, we simultaneously acquired images of the antigen-force sensors opening and IRM images and merged the two. LZ GC B cells exerted force on the sensors beginning approximately 5 min after the cells were placed on the sensor-containing PLBs and the opening of the sensors was restricted to the areas of contact of the LZ GC B cell's pod-like structures with the membrane (Fig. 2E and Movie S5). Thus, we conclude from the data presented thus far that in LZ GC B cells both BCR signaling and exertion of a pulling force through the BCRs occur in novel F-actin and ezrin-rich pod-like structures.

Behavior of GC B Cells in Response to Antigen is Dictated by Intrinsic Affinity Thresholds.

We determined whether the differences observed in BCR organization and signaling properties for naïve and GC B cells correlated with their ability to discern affinity for membrane-associated antigens. As surrogate antigen we used κ-specific monoclonal antibodies (anti-κ mAbs) that were generated in mice to either rat κ chains and showed a low-affinity for human κ chains (KD = 3.9×10^{-7}) as determined by Biacore surface plasmon resonance analysis or were generated in mice to human κ chains and showed a high-affinity for human κ chains (KD = 2.4

$\times 10^{-9}$). Streptavidin conjugated anti-κ mAbs were bound to PLBs that contained biotinylated lipids. Lambda light chain-expressing B cells were removed from purified naive B cell and LZ GC B cell sub-populations by negative sorting. The κ light chain-expressing LZ GC and naïve B cells were placed on PLBs that contained low- or high-affinity anti-κ mAbs for 7 or 25 min. Cells were permeabilized and stained with antibodies specific for the phosphorylated forms of the BCR's Igα chain, CD79a (pCD79A), and several components of the B cell signaling cascade including Syk (pSyk), BLNK (pBLNK) and PLCγ2 (pPLCγ2). Cells were imaged by TIRFM and the MFI in the contact areas between the B cell and the antigen-containing PLBs was quantified.

The TIRFM images showed that naïve B cells formed immune synapses similarly on both the high and low-affinity antigen-containing PLBs (Fig. 3A) and accumulated similar amounts of BCR in the area of contact between the B cell and the PLB in response to low and high-affinity antigens at 7 min (Fig. 3B). At 25 min the accumulation of the BCR was less for low versus high-affinity antigens, nonetheless the accumulation was significantly greater than that of resting naïve B cells (Fig. 3B). In contrast, LZ GC B cells did not form stable contacts with the low-affinity antigen-containing bilayers (Fig. 3A) nor did they accumulate BCRs in the contact area between the B cell and the PLBs to an amount that was significantly greater than that accumulated by resting LZ GC B cells placed on bilayers that did not contain antigen (Fig. 3B). When placed on the high-affinity antigen-containing PLBs, LZ GC B cells accumulated BCRs in a punctate pattern (Fig. 3A). The amount of LZ GC BCRs that accumulated in the interface between the B cell and the high-affinity antigen-containing PLB was significantly greater than that of resting LZ GC B cells not exposed to antigen although less than that of naïve B cells (Fig. 3B).

Quantification of the phospho-signaling components in the contact area of the B cells with the bilayers showed a similar pattern. Naïve B cells induced phosphorylation of CD79a, Syk, BLNK and PLCγ when placed on either low-affinity or high-affinity antigen-containing PLBs (Fig. 3C-3F). In contrast, LZ GC B cells were unable to initiate phosphorylation of signaling components in response to low-affinity antigen-containing PLB (Fig. 3C-3F) but responded to high-affinity antigen-containing PLB. Taken together these results establish that LZ GC B cells have a higher antigen affinity threshold for activation as compared to naïve B cells.

To obtain a dynamic view of the responses of B cells to high- versus low-affinity antigen we acquired DIC and IRM images of live LZ GC and naïve B cells engaging PLBs containing low- versus high-affinity anti-κ mAbs. Shown are both the DIC and IRM images (Fig. 3G and Movie S6) as well as quantitative analyses of both the IRM and DIC images displayed as kymographs (Fig. 3H). The images revealed dramatic differences between the response to high- versus low-affinity antigens by naïve B cells and LZ GC B cells. High-affinity antigens immobilized naïve B cells in stable large contact areas with the PLB (Fig. 3G and Movie S6) as quantified in the kymograph (Fig. 3H). In contrast, naïve B cells on low-affinity antigen-PLB formed smaller contact areas and continued to extend membrane ruffles around the periphery presumably continuing to search for antigen (Fig. 3G and Movie S6) as indicated by red arrow heads in the kymograph (Fig. 3H). LZ GC B cells placed on high-affinity antigen-containing PLB vigorously explored the PLB through their peripheral pods (Fig. 3H and Movie S6). However, with time their pod formed stable contacts with the PLB as indicated by the red arrow heads in the kymograph (Fig. 3H). Low-affinity LZ GC B cells failed to form stable contacts with the membranes but rather continued to make highly dynamic contacts with the PLBs (Fig. 3G, 3H and Movie S6) even occasionally moving over the PLB (Movie S7). Thus, the behavior

of the B cells on the antigen-containing bilayers appears to be dictated by the B cells' affinity for antigen.

To quantify the movement of pod-like structures in the DIC images, individual pod-like structures on PLBs were identified and their movement was measured using a particle tracking algorithm (fig. S4B). During the early stage of contact, LZ GC B cells engaged with high-affinity antigen moved their pods more vigorously in a broader area (median diffusion $2.5x10^{-3}$ um^2/sec) relative to LZ GC B cells engaged with low-affinity antigen (median diffusion $1.7x10^{-3}$ um^2/sec) (Fig. 3I). Movement of pod-like structures markedly slowed during the late stage of contact for LZ GC B cells engaged with high-affinity antigen (median diffusion $1.0x10^{-3}$ um^2/sec) relative to earlier time points and to LZ GC B cells engaged with low affinity antigen (median diffusion $1.3x10^{-3}$ um^2/sec) (Fig. 3I), indicating that as more BCRs engage with high-affinity antigen, pod movement stabilizes.

In addition, the behavior of LZ GC B cells on the low-affinity antigen is strikingly different from that of LZ GC B cells that contacted PLB that contain no antigen (Fig. 1A) indicting that the searching behavior of LZ GC B cells can be triggered by interactions with antigens that are of too low an affinity to stimulate robust signaling.

Extraction and Trafficking of Membrane Associated Antigen Distinguishes GC B cells

Current evidence indicates that the B cell's affinity for antigen is ultimately tested by the B cell's ability to internalize, process and present antigen to Tfh cells (*23*). Consequentially, we tested the ability of human GC B cells and naïve B cells to extract antigen from pliant plasma membrane sheets (PMS) presenting either high- or low-affinity anti-κ mAbs. Total purified human tonsil B cells were incubated on PMS coated with fluorescently labeled high- or low-

affinity anti-κ for 2 h and the B cells were harvested and analyzed by flow cytometry to identify B cells that had acquired fluorescent antigen and within this population to identify naïve B cells and GC B cells (Fig. 4A). Analysis of the antigen-positive B cells recovered from the PMS showed that the percent of naïve B cells that acquired antigen from the high-affinity PMS were similar to the percent that acquired antigen from the low-affinity PMS. In contrast, significantly fewer GC B cells acquired antigen from the low-affinity PMS as compared to the high-affinity PMS (Fig. 4A). Thus, GC B cells have a greater affinity threshold for antigen extraction as compared to naïve B cells.

We characterized the patterns of trafficking and internalization of membrane associated antigen captured by BCRs of LZ GC B cells and naïve B cells placed on PLB that contained Atto 633-labeled antigen, fixed, permeabilized, and stained with Alexa Fluor 488-conjugated phalloidin. As observed in longitudinal sections of naïve B cells, antigen-bound BCRs accumulated in the plane of the contact area with the PMS in the center of the synapse where they were internalized (Fig. 4B and Movie S8). No cell surface associated antigen was detected outside of the contact area as shown in the 3D surface reconstruction (Fig. 4B). In contrast, LZ GC B cells engaged antigens via pod-like structures and trafficked antigen away from the contact area along the sides of the cells to distal sites for internalization (Fig. 4B and Movie S8). To determine the polarity of the cells we located the microtubule organizing centers (MTOCs) using γ tubulin-specific antibodies in naïve and LZ GC B cells after activation on antigen-containing PMS. In the majority of activated naïve B cells MTOCs were polarized and located proximal to PMS (Fig. 4C). In contrast, MTOCs in activated LZ GC B cells were not polarized toward the PMS and appeared to be dispersed large distances from the PMS (Fig. 4C).

BCR-mediated antigen internalization in B cells is primarily by clathrin-mediated endocytosis (CME) (*32*). Sorting nextin (SNX) 9 and SNX18 are key components of the endocytosis machinery and modulators of CME (*33-35*). By flow cytometry, the expression of both SNX9 and SNX18 was four to six fold higher in naïve B cells as compared to LZ GC B cells (fig. S5A and S5B). By confocal microscopy in naïve B cells both SNX9 and SNX18 were concentrated with antigen in the immune synapse (Fig. 4D), polarized toward the antigen-containing PMS as shown and quantified in longitudinal sections (Fig. 4D and fig. S5C-S5E). In striking contrast, in LZ GC B cells SNX9 and SNX18 showed no pattern of accumulation but rather were dispersed throughout the cell (Fig. 4D). In addition, 3D reconstructions of images of α-tubulin, SNX9 or 18 and antigen clearly showed the polarization of α-tubulin and SNX9 and 18 toward the contact area of naïve B cells with the antigen-containing PLB and antigen internalization from the contact site (Fig. 4E and Movie S9). In contrast, α-tubulin and SNX9 and 18 were not polarized in LZ GC B cells and the antigen was trafficked along the outside of the cell to distal sites (Fig. 4E and Movie S9).

It has been shown, primarily in naïve mouse B cells, that extracted antigens are internalized and trafficked to specialized LAMP-1$^+$ MHC class II-containing late endosomes (MIIC) which contain various proteases and reductases for efficient antigen processing (*36*). In activated naïve B cells LAMP-1$^+$ vesicles were polarized toward the immune synapse and antigens gathered by BCRs were highly colocalized with LAMP-1$^+$ vesicles (Fig. 4F and Movie S10). LAMP-1$^+$ vesicles in LZ GC B cells were less polarized and less antigen was colocalized with LAMP-1$^+$ vesicles. This result suggests that as compared to naïve B cells, LZ GC B cells do not efficiently traffic extracted antigens to LAMP-1$^+$ MIIC compartments.

We next followed the trafficking of antigen internalized by naïve B cells and LZ GC B cells with time. Unsorted purified tonsil B cells were incubated on PMS containing DyLight 650-conjugated $F(ab')_2$ anti-λ/κ and the pH-sensitive dye, pHrodo, the FI of which increases with increasing pH. Cells were removed from the PMS and analyzed by flow cytometry to identify naïve B cells and LZ GC B cells and to quantify the DyLight 650 and pHrodo FI. In controls in which the PMS contained DyLight 650-conjugated BSA and pHrodo, no DyLight 650 or pHrodo FI was detected in naïve and LZ GC B cells (Fig. 4G). Between 30 and 120 min on the PMS the amount of antigen associated with naïve and LZ GC B cells increased as did the pHrodo FI, however, the temporal patterns of antigen up-take and pHrodo FI differed between naïve and LZ GC B cells (Fig. 4G). Overlapping the data in Fig. 4G it is apparent that naive B cells extracted more antigen with time as compared to LZ GC B cells (fig. S5F) and trafficked a larger portion of the acquired antigen to acidic compartments as indicated by increased pHrodo FI. Comparing naïve B cells to LZ GC B cells that acquired equivalent amounts of antigen at 120 min, it was clear that naïve B cells trafficked a larger portion of the antigen to acidic compartments: over 80% of naïve B cells were pHrodo positive as compared to 20% of LZ GC B cells and the pHrodo FI was higher for naïve B cells as compared to LZ GC B cells (Fig. 4H).

Human LZ GC B Cells Express IRF-4 in Response to High-Affinity Antigen in Combination with Tfh Cell Help

Both LZ GC and naïve B cells pass through checkpoints in which the presentation of antigen to T cells dictates one of several fates including differentiation into long- and short-lived PCs. We characterized the response of naïve and LZ GC B cells to high versus low-affinity membrane bound antigens in the presence or absence of CD40-specific mAb, IL-4 and IL-21 to

mimic Tfh cell help. We quantified the expression of IRF-4, a gene required for PC differentiation and found that LZ GC B cells increased transcription of IRF-4 modestly in response to high but not low-affinity antigens (Fig. 5A). However, the largest increase in IRF-4 expression was in response to a combination of high-affinity antigen and Tfh cell help. These data demonstrate that the trigger for maximal GC B cell differentiation to PCs is both antigen affinity-dependent and dependent on Tfh cell help.

In contrast to LZ GC B cells, naïve B cells expressed IRF4 equivalently in response to both high and low-affinity antigens (Fig. 5B). Tfh cell help independently induced IRF4 expression and augmented the IRF4 expression to both low and high-affinity antigens. Taken together these data provide evidence that the high-affinity threshold for activation of LZ GC B cells as compared to naïve B cells has the functional outcome of maximally triggering high-affinity LZ GC B cells to differentiate to PCs in the presence of Tfh cell help.

The Differential Expression of Surface Markers may Further Contribute to Affinity Discrimination by Human GC B Cells

To determine if GC B cells differ from naïve B cells in the expression of cell surface molecules that could contribute to affinity discrimination we carried out an analysis of over 330 B cell surface markers on resting and antigen-activated naïve B cells, DZ and LZ GC B cells and MBCs for comparison. The data are expressed as a heat map comparing LZ and DZ GC B cells and MBCs to naïve B cells (Fig. 6A and fig. S6). LZ GC and DZ GC B cells showed nearly identical cell surface expression profiles with the exception of a few previously reported markers including CD83, CD86, and CXCR4. In contrast, the cell surface expression of markers on MBC more closely resembled that of naïve B cells. The differential expression of several B cell surface

markers by GC B cells is of potential interest, including: the tetraspanins CD9, 53, 63 and 81; CD1a; BAFF-R and TACI. Notably, many environmental sensing co-receptors involved in the regulation of BCR signaling were down-regulated in GC B cells including FcεRII, FcγRII, CR1, SIGLEC-2, PECAM-1 and CR2, suggesting that the response of GC B cells to antigen may be minimally influenced by environmental signals.

Integrins were also differentially expressed by GC B cells as compared to naïve B cells and given their importance in B cell activation, we quantified the expression levels of a variety of human integrins and found a significant difference between naïve B cells and LZ GC B cells in their expression of integrin alpha 4, alpha M, beta 1 and beta 7 (Fig. 6A, fig. S7A, and S7B). We further characterized VLA-4 expression as it plays a key role in stabilizing the initial interaction of B cells with antigens associated on the surface of APCs that express its ligand, VCAM-1 (*37*). VLA-4/VCAM-1 interactions also facilitate B cell activation following BCR antigen binding (*37*). As compared to naïve B cells, the surface expression of the VLA-4 chains CD29 (β1) and CD49d (α4) was greatly reduced on LZ GC B cells (Fig. 6B and 6C). VLA-4 undergoes an important conformational change via an inside-out signaling pathway to switch from a low-affinity to high-affinity active state, that increases its affinity for VCAM-1 by ~100 fold (*37*). Using an antibody specific for VLA-4 in the high-affinity state we found that LZ GC B cells also expressed less active-state VLA-4 as compared to naïve B cells (Fig. 6B and 6C).

To determine if the decreased expression of VLA-4 resulted in a reduced ability of GC B cells to adhere to VCAM-1 on surfaces, we incubated unsorted purified tonsillar B cells with an excess of VCAM-1-coated magnetic agarose beads at 37°C for 20 min and analyzed the composition of bead-bound and unbound B cells by flow cytometry. The vast majority of B cells that bound to the VCAM-1 beads were naïve B cells (Fig. 6D). GC B cells were nearly

exclusively recovered in the unbound fraction indicating that the low expression of VLA-4 on GC B cells had the functional consequence of limiting the ability of GC B cells to engage VCAM-1 surfaces. Taken together these results suggest that GC B cells may be highly dependent on BCR-antigen interactions in the absence of strong integrin mediated cell-cell contact with antigen presenting cells.

Discussion

Affinity maturation of antibody responses is a central feature of immunological memory. Indeed, the ability to drive affinity maturation is a critical requirement of all effective vaccines. We now appreciate that high-affinity B cells are selected in GC LZs in a competitive process in which Tfh cells provide help to B cells based on B cell signaling and on the amount of antigen B cells are able to gather from FDC surfaces, internalize, process and present to Tfh cells. A BCR signaling/antigen-processing presentation checkpoint also exists for naïve B cells to gain entry into the GC. We sought to determine whether human GC B cells and naïve B cells were similarly able to discriminate their affinity for antigen and if the structures and mechanisms underlying affinity discrimination and antigen presentation were similar. We determined that human GC B cells have a higher antigen affinity threshold for signaling through the BCRs, for extracting and trafficking antigen from membranes, for processing and for differentiation into PCs. The cellular processes through which GC B cells engaged antigen and extracted and internalized it for processing were remarkably distinct from the processes used by naïve B cells. We also provided evidence for a variety of additional differences between GC B cells and naïve B cells that together could further contribute to establishing antigen affinity thresholds.

One of the most striking features of LZ GC B cells is their cellular architecture. We provided evidence that on LZ GC B cells BCRs are concentrated in novel, highly dynamic, ezrin- and actin-rich pod-like structures through which the BCRs engage antigen, signal, exert pulling forces and extract antigen from membranes. In contrast, the BCRs on naïve B cells function in flat, stable contacts with antigen-containing surfaces displaying the well-described features of immune synapses and cSMACs. These observations raise the question of the function of the BCR-containing structures. The LZ GC B cells' pod-like structures may serve to isolate small numbers of BCRs in a given area and thus decrease the avidity of the BCRs for membrane bound antigen and force the B cells to function through only monomeric affinity-dependent interactions. To this point, we earlier demonstrated that B cells can be readily activated through interactions with antigen monomers on membranes (*38*). A reliance on monomeric interactions would contribute to the high-affinity thresholds for LZ GC B cell signaling and antigen extraction. In contrast, naïve B cells were able to extract both high- and low-affinity antigens from PMS. The large flat contact area of the naïve B cells with the antigen-containing PLB may increase the number of engaged BCRs and consequently increase the avidity of the BCRs for the antigen and thus increase the probability that patches of antigen will be pulled into the cells overriding the limitations of affinity. Along a similar vein some BCR signaling molecules, such as Syk, have been shown to have trans-activity (*39*) which enables propagation of a signal from activated BCRs to BCRs present in large-scale cSMACs clusters, such as those formed by naïve B cells. This trans-activity could amplify the BCR signaling allowing B cell activation even to low-affinity antigens. The pod-like structures could function to insulate populations of BCR-antigen clusters from each other so that they could not benefit from trans-acting signaling activity. On a larger scale, the dynamic nature of these pod-like structures may underlie the rapid

scanning behavior of LZ GC B cells over FDC observed *in vivo* in mice (*9*). When activated or confronting a spatial gradient of antigen or under the influence of a chemokine gradient the GC B cells may 'walk' on the pod-like structures searching for antigen.

SEM analysis showed additional features of the architecture of LZ GC B cells that could contribute to antigen sensing. As compared to naïve B cells, LZ GC B cells display a distinct cell morphology in both resting and activated states, with corrugated, wrinkled membrane topology. This topology may provide an increased surface area for membrane-mediated events such as adhesion and sensing (*40, 41*). This wrinkled surface morphology may also permit LZ GC B cells to undergo the large deformations of the membrane required for the formation of pod-like structures.

We observed that the pod-like structures of LZ GC B cells moved differently with time when placed on low- versus high-affinity antigens. The LZ GC B cells engaging high-affinity antigen moved their pods more vigorously in broader areas as compared to LZ GC B cells engaging low-affinity antigen. This suggests that LZ GC B cells modulate their search for antigen in response to BCR affinity, which may further enhance affinity discrimination.

It will be of interest in future studies to understand in greater depth the mechanisms by which MBCs that have undergone selection in GCs engage antigen. Wang *et al.(42)* recently reported that in mice GCBs expressing IgG BCRs generated greater traction forces on membrane-associated antigen during the initiation of activation than did naïve B cells consistant with increased expression of motor proteins in MBCs. Preliminary results from our studies are consistent with this observation showing that MBCs were able to exert pulling force on membrane-associated antigen that was sufficient to open 9 pN DNA force sensor whereas naïve

B cells were not. How this function of MBCs might contribute to affinity discrimination remains to be determined.

In addition to the differences in the antigen affinity threshold for antigen extraction between naïve B cells and LZ GC B cells, we also observed a striking difference in the internalization and the intracellular trafficking of antigen to acidic compartments for processing. Naïve B cells polarized the MTOC to the contact area of the cell with the antigen-containing bilayer and internalized antigen from this area. We observed that the majority of internalized antigen was in close proximity to SNX9 and SNX18 as well as LAMP-1$^+$ vesicles. SNX9 and SNX18 are composed of Src homology 3 (SH3), phox homology (PX), and Bin-amphiphysin-Rvs (BAR) domains and play distinct roles during endocytosis. BAR domains form hetero- or homodimers with a bent structure which is optimal for binding to curved membrane structures and the SH3 domains interact with numerous key molecules required to complete CME (*43*). In contrast, LZ GC B cells express very little SNX9 and SNX18 and do not polarize the SNXs, MTOC and LAMP-1$^+$ vesicles to the contact area with the antigen-containing bilayer and LZ GC B cells do not internalize antigen through the contact area. Rather GC B cells traffic BCR-bound antigen away from the contact area to distal sites where antigen is internalized. Similar trafficking patterns have been observed in mouse GC and naïve B cells (*26*). Thus, it appears that LZ GC B cells and naïve B cells rely on different endocytic processes for antigen internalization and may not have identical LAMP-1$^+$ compartments in which processing occurs. We also observed that naïve B cells acquired more antigen with time as compared to GC B cells and delivered a greater portion of their acquired antigen to acidic compartments for processing. In contrast, only a small portion of GC B cells that have acquired a similar amount of antigen were able to traffic antigen into acidic compartments. The high threshold for processing of internalized

antigen may provide a mechanism by which GC B cells can temporally or spatially regulate the presentation of antigen to Tfh cells during GC LZ competition.

Based on our new findings we predict different outcomes for naïve B cells and LZ GC B cells upon immunization or infection *in vivo*. Even low-affinity naïve B cells that are able to effectively extract, internalize and traffic low-affinity antigens would have the potential to receive Tfh cell help and differentiate to GC B cells and undergo affinity maturation. Thus, the naïve B cell repertoire may not be highly selected at the first checkpoint but rather may maintain a broad antigen specificity repertoire. In contrast, only high-affinity LZ GC B cells would be able to acquire antigen for presentation to Tfh cells for positive selection. Presumably, the well documented competition of LZ GC B cells for antigen and Tfh cells would occur among those LZ GC B cells that exceeded the minimal antigen affinity threshold. Our strategy to produce high versus low-affinity surrogate antigens for human B cells, namely by generating mAbs in mice to human κ chain versus rat κ chain provided only two κ-specific mAbs that differed approximately 60 fold in the lower range of possible antibody affinities. It will be of interest to develop additional reagents that allow a more precise assessment of the degree of affinity discrimination of these two human B cell subsets.

In terms of the outcome of LZ GC B cell encounter with antigen, we demonstrated that human LZ GC B cells increased IRF-4 transcription in response to BCR stimulation or Tfh like stimuli alone, but optimal IRF-4 expression was induced only when two stimuli were given. In mice it has been shown that sustained high expression of IRF4 promote PC differentiation (*44-47*). Our observation is consistent with the findings of Krautler *et al.* (*23*) that provided evidence in mice for a two-signal mechanism in the differentiation of LZ GC B cells to PCs, the first provided by antigen and the second by Tfh cells. IRF-4 is also an important fate-decision factor

for naïve B cells. We showed that the increase in IRF-4 expression in naïve B cells is relatively affinity independent and more highly dependent on Tfh cell help. This observation suggests that low-affinity B cells may capture sufficient antigen to activate Tfh cells to allow differentiation directly to short-lived PCs. If so, the short-lived PCs would produce antibodies that are not highly affinity selected. The cell surface expression level of CD40, IL4R, and IL21R in GC B cells was slightly higher than naïve B cells (fig. S6C) and IRF4 mRNA expression was induced more in GC B cells compared to naïve B cells when Tfh like stimuli alone was given however synergistic effect on the induction of IRF4 mRNA expression with high affinity antigen was only seen in GC B cells suggesting depending on antigen affinity GC B cells are able to differentially express IFR4 mRNA even under robust Tfh like stimuli.

We also provided evidence that as compared to naïve B cells, LZ GC B cells express less BCR of all isotypes on their surfaces suggesting that GC B cells may be inherently more sensitive to the concentration and affinity of antigen as compared to naïve B cells. We showed that as compared to naïve B cells human LZ GC B cells express very little VLA-4 which is unique in human GC B cells as mouse GC B cells show comparable surface expression level of VLA-4 in comparison with naïve B cells.(*48*) VLA-4 is an integrin that binds to its ligand, VCAM-1, expressed by FDCs that present antigen to LZ GC B cells and serves to lower the affinity threshold for BCR signaling. We demonstrated the reduced expression of VLA-4 on GC B cells resulted in a reduced ability of LZ GC B cells to interact with VCAM-1 coated surfaces as compared to naïve B cells. Based on these observations we predict that differences in the ability of LZ GC B cells and naïve B cells to discriminate the affinity of antigen may be even greater when B cells encounter antigen on VCAM-1 expressing APCs *in vivo* than demonstrated here *in vitro* in the absence of VCAM-1. It is of interest that in contrast to VLA-4 the expression

of which was decreased on LZ GC B cells as compared to naïve B cells, the levels of expression of LFA-1 were similar for LZ GC B cells and naïve B cells. LFA-1 is an integrin that both stabilizes B cell interactions with APCs and plays a critical role in B cell-T cell interactions (*49*). This suggests that once LZ GC B cells succeed in triggering BCR signaling in a mostly VLA-4-independent fashion, the GC B cells will not be compromised in subsequent LFA-1-dependent processes, including interactions with Tfh cells.

Our studies presented here provided evidence for intrinsic properties of LZ GC B cells that may contribute to enhanced affinity discrimination. Further elucidating the mechanisms of affinity discrimination may provide new strategies for the development of vaccines which require the generation of affinity-matured antibody responses.

Materials and Methods

Purification and sorting of human tonsillar B lymphocytes

Tonsils were obtained from patients undergoing tonsillectomies. The tonsillar tissue was cut into small pieces, and cells were harvested in media containing RPMI medium 1640, 10% FBS, sodium pyruvate, L-glutamine, non-essential amino acids, Penn-strep, HEPES, and beta-mercaptoethanol (RPMI-10) with gentle tapping. The tonsillar cells were then filtered through cell strainers with 70 micron pores to obtain single cell-suspensions. Tonsillar B cells were isolated by negative selection using the EasySep Human B cell enrichment kit (STEMCELL) and, when required, were further sorted using DyLight 405 (Innova Biosciences) conjugated anti-IgD Fab (SouthernBiotech), BV786 anti-CD10 (BD Biosciences), PE anti-CD184 (BD Biosciences), and DyLight 488 (Innova Biosciences) conjugated anti-λlight chain Fab (SouthernBiotech) with a FACSAria II cell sorter (BD Biosciences).

TIRF microscopy

PLBs were prepared as described previously (*50*). Sorted cells were stained with either Alexa Fluor 488 or Alexa Fluor 647 anti-IgM Fab antibodies (Jackson ImmunoResearch) for naïve and IgM GC B cells or Alexa Fluor 488 or Alexa Fluor 647 anti-IgG Fab antibodies (Jackson ImmunoResearch) for IgG GC B cells, placed on PLB presenting goat $F(ab')_2$ anti-human Igκ (SouthernBiotech) and anti-human Igλ (SouthernBiotech) surrogate antigens or without antigen. They were then incubated at 37°C for the times indicated, fixed in 4% PFA, permeabilized in saponin, and stained with either pSyk-specific antibodies (Cell Signaling), Alexa Fluor 647 labeled pPLCγ2-specific antibodies (BD Biosciences), pPI3K-specific antibodies (Cell Signaling), pBtk-specific antibodies (Cell Signaling), DyLight 650 (Innova Biosciences)

conjugated pVav-specific antibodies (Abcam), DyLight 488 (Innova Biosciences) conjugated pCbl-specific antibodies (Santa Cruz Biotechnology), or pSHP-1-specific antibodies (Cell Signaling). For cells stained with primary antibodies, Alexa Fluor 488 secondary antibodies (Invitrogen) were used as detecting reagents. Images were acquired by Olympus IX-81 TIRF microscope system. To analyze the levels of phosphorylated signaling molecules, MFI values of pSyk, pPLCγ2, pPI3K, pBtk, pVav, pCbl, or pSHP-1 within the immune synapse were analyzed by MatLab (MathWorks) software. The Pearson's correlation coefficients of signaling molecules and BCR were calculated from background-subtracted images by MatLab (MathWorks). Time-lapse live cell TIRF imaging was done at 37°C on a climate-controlled stage with 5% CO_2 and 75% humidity. Naïve B cells were stained with Alexa Fluor 647 anti-IgM Fab (Jackson ImmunoResearch) and DyLight 488 (Innova Biosciences) conjugated anti-CD19 (Biolegend) Fab while LZ GC and DZ GC B cells were stained with Alexa Fluor 647 anti-IgG Fab (Jackson ImmunoResearch) and DyLight 488 (Innova Biosciences) conjugated anti-CD19 (Biolegend) Fab. Each B cell subset was placed on PLBs containing goat $F(ab')_2$ anti-human Igκ (SouthernBiotech) and anti-human Igλ (SouthernBiotech) surrogate antigen and TIRF images were acquired at 6 sec intervals for 20 min. The Pearson's correlation coefficient (R) of CD19 and BCR were calculated from background-subtracted images by MatLab (Mathworks). For time-lapse live cell DIC and IRM TIRF imaging, naïve and LZ GC B cells were placed on PLB presenting Alexa 647 goat $F(ab')_2$ anti-human Igκ (SouthernBiotech) and anti-human Igλ (SouthernBiotech) surrogate antigens or without antigen and incubated at 37°C on a climate-controlled stage with 5% CO_2 and 75% humidity, and TIRF images were acquired at 3 sec intervals for 15 min after activation.

For the affinity discrimination experiment using high and low-affinity antigen, Igκ$^+$ naïve and LZ GC B cells were stained with DyLight 488 anti-IgM Fab (Jackson ImmunoResearch) for naïve B cells or DyLight 488 anti-IgG Fab (Jackson ImmunoResearch) for GC B cells, placed on PLBs either presenting anti-human Igκ, anti- rat Igκ antibodies, or without antigen. They were then incubated at 37°C for the times indicated in the figure legends, fixed in 4% PFA, permeabilized with saponin, and stained with anti-pCD79A (Cell Signaling), anti-pSyk (Cell Signaling), Alexa Fluor 647 anti-pBLNK (BD Biosciences), or Alexa Fluor 647 anti-pPLCγ2 (BD Biosciences). Primary anti-pCD79A (Cell Signaling), anti-pSyk (Cell Signaling) antibodies were labeled with Alexa Fluor 647 secondary antibodies (Invitrogen) for cell staining. For time-lapse live cell imaging, Igκ$^+$ naïve and LZ GC B cells were placed on PLB presenting anti-human Igκ or anti- rat Igκ antibodies surrogate antigens and incubated at 37°C on a climate-controlled stage with 5% CO_2 and 75% humidity, and DIC and IRM images were acquired at 3 sec intervals for 15 min. Image acquisition and analysis was performed in the same method as previously described.

Measurement and analysis of BCR cluster growth

Naïve and GC B cells were isolated and sorted from tonsil, and their BCRs were labeled with Alexa Fluor 488 anti-IgM (Jackson ImmunoResearch) Fab for naïve B cells, or with Alexa Fluor 488 anti-IgG Fab (Jackson ImmunoResearch) for GC B cells. Time-lapse live cell TIRF imaging was performed at 37°C on a heated stage with 5% CO_2 gas supply and 75% humidity. Each B cell subset was placed on PLBs containing goat F(ab')$_2$ anti-human Igκ (SouthernBiotech) and goat F(ab')$_2$ anti-human Igλ (SouthernBiotech) surrogate antigen, and images were acquired at 3 sec intervals for 20 min. BCR cluster growth was measured by MatLab (MathWorks).

Measurement and analysis of Ezrin, SNX9, SNX18, LAMP-1 and surface VLA-4 and LFA-1 expression

Purified tonsillar B cells from five different individuals were stained with near-IR Live/Dead marker (ThermoFisher), DyLight 405 (Innova Biosciences) conjugated anti-IgD Fab (SouthernBiotech), BV786 anti-CD10 (BD Biosciences), PE anti-CD184 (BD Biosciences), Alexa Fluor 488 anti-CD29 (Biolegend), Alexa Fluor 647 anti-CD49d (Biolegend), DyLight 488 (Innova Biosciences) anti-VLA-4 active epitope (EMD Millipore), PE-Cy7 anti-CD11 (Biolegend), or FITC anti-CD18 (Biolegend) on ice, washed, and the amount of signal was quantified by flow cytometry (BD LSR II) and Flow cytometry data was analyzed with FlowJo (FLOWJO, LLC) and Prism (GraphPad) software.

For Ezrin, SNX9, SNX18, and LAMP-1 staining, purified tonsillar B cells from five individuals were stained with near-IR Live/Dead marker (ThermoFisher), DyLight 405 (Innova Biosciences) conjugated anti-IgD Fab (SouthernBiotech), BV786 anti-CD10 (BD Biosciences), PE anti-CD184 (BD Biosciences) on ice, washed, and stained cells were fixed and permeabilized using BD Cytofix/Cytoperm (BD Biosciences) following manufacturer's protocol. Stained cells were incubated with anti-Ezrin (Cell Signaling), anti-SNX9 (Sigma), anti-SNX18(Sigma), or DyLight 550 (Innova Biosciences) conjugated anti-LAMP-1 (Abcam) antibodies at room temperature for 2 h, washed. For Ezrin, SNX9, and SNX18, cells were stained with Alexa Fluor 647 secondary antibodies (Invitrogen), washed, and the amount of signal was quantified by flow cytometry (BD LSR II) and Flow cytometry data was analyzed with FlowJo (FLOWJO, LLC) and Prism (GraphPad) software.

VCAM-1 binding assay

30ul of Nickel Agarose magnetic beads (Sigma) were washed and incubated with either 100ug of recombinant human VCAM-1 Fc chimera proteins (R&D Systems) or purified human IgG (MP biomedicals) for 4 h in diH_2O containing 0.1% BSA, 50mM Tris-HCl pH 8.0, 10mM imidazole, and 100mM NaCl (washing buffer). They were then washed in HBSS containing 0.1% BSA, 10mM imidazole, 100mM NaCl (binding buffer). Negatively-isolated tonsillar B cells in binding buffer were mixed with nickel agarose magnetic beads and incubated on a tube rotator at 37°C for 30 min. Unbound cells were collected using a magnetic separation stand and bound cells were eluted with HBSS containing 150mM imidazole (Sigma) elution buffer after washing. Bound and unbound B cells, as well as a control that had not been incubated with beads, were stained on ice for 20 min using near-IR Live/Dead marker (ThermoFisher), FITC anti-IgD (Miltenyi), and BV421 anti-CD10 (BD Biosciences) and the amount of signal was measured by flow cytometry (BD LSR II) and Flow cytometry data was analyzed with FlowJo (FLOWJO, LLC) and Prism (GraphPad) software.

STED, SEM, and confocal microscopy

Cells were placed on PLBs containing goat $F(ab')_2$ anti-human Igκ (SouthernBiotech) and goat $F(ab')_2$ anti-human Igλ (SouthernBiotech) surrogate antigen at 37°C for 25 min, fixed in 4% PFA, and permeabilized in saponin. For super resolution images of F-actin structure in the immune synapse, cells were stained with Alexa Fluor 488 phalloidin (ThermoFisher) and images were acquired with STED microscopy (Leica). For immune synapse and z-stack images of F-actin and BCR, cells were labeled with Alexa Fluor 647 anti-IgM or anti-IgG Fab and were activated in the same manner as cells for STED images. Images were obtained using a Zeiss-880

confocal microscope and stacked images were deconvolved with Huygens Software (Huygens Software). For z-stack images of F-actin, ezrin, and BCR, LZ GC B cells were labeled with Alexa Fluor 647 anti-IgG Fab and were activated in the same manner as cells for STED images and images were obtained using a Zeiss-880 confocal microscope. The MFI and the Pearson's correlation coefficients of ezrin and F-actin were calculated from background-subtracted images by Zen software (Zeiss). For z-stack images of SNX9, SNX18, LAMP-1, and MTOC, naïve and LZ GC B cells were placed on PMS containing DyLight 650 (Innova Biosciences) conjugated goat $F(ab')_2$ anti-human Igκ (SouthernBiotech) and anti-human Igλ (SouthernBiotech) surrogate antigen and incubated at 37°C for 25 min or 45 min, and fixed in 4% PFA. Fixed cells were permeabilized in saponin and stained with Alexa Fluor 488 phalloidin (ThermoFisher), and anti-Ezrin (Cell signaling), anti-SNX9 (Sigma), anti-SNX18 (Sigma), anti-LAMP-1 (Abcam), anti-alpha tubulin, or anti-gamma tubulin at 4°C overnight. They were washed, stained with Alexa Fluor 550 secondary antibodies (Invitrogen), and washed. Images were obtained using a Zeiss-880 confocal microscope. Distance of MTOC, SNX9, and SNX18 cluster to PMS, and MFI and TFI of SNX9 and SNX18 per each z-stack were measured by ImageJ (NIH). 3D images and movies of SNX9, SNX18, LAMP-1 and colocalization of antigen with LAMP-1 were generated by Imaris (Bitplane).

For SEM images, cells were activated on PLBs coated with goat $F(ab')_2$ anti-human Igκ (SouthernBiotech) and goat $F(ab')_2$ anti-human Igλ (SouthernBiotech) surrogate antigen, or without antigen at 37°C for 25 min. Coverslip cultures were fixed in a 2.5% glutaraldehyde, 1% paraformaldehyde, and 0.1M sodium cacodylate buffer with a pH of 7.4. The coverslips were then rinsed in cacodylate buffer, postfixed with 1% OsO_4 in the same buffer, dehydrated in an ethanol series, and dried using a Samdri-795 critical point dryer (Tousimis Research Corp,

Rockville MD). The dried coverslip cultures were coated with 5nm of gold in an EMS 575-X sputter coater (Electron Microscopy Sciences, Hatfield PA) and imaged with a Hitachi S-3400 N1 scanning electron microscope (Hitachi High Technologies America, Inc., Pleasanton CA).

IRM

Time-lapse live cell TIRF IRM imaging was done at 37°C on a heated stage with 5% CO_2 gas supply and 75% humidity. Each B cell subset was placed on PLBs containing goat $F(ab')_2$ anti-human Igκ (SouthernBiotech) and goat $F(ab')_2$ anti-human Igλ (SouthernBiotech) surrogate antigen, and images were acquired at 3 sec intervals for 20 min.

MATLAB algorithms were developed to perform robust and automated image analysis to produce the following figures. We inverted the grayscale IRM signal in each image in order to positively correlate the proximity to the coverslip with the intensity values, and subtracted background. To measure the proximity to the coverslip from the center to the periphery of the area of interaction of naïve and LZ GC B cells, each cell was analyzed with the graph on the left representing the quantitative data of the naïve B cell and the one on the right corresponding to the quantitative data of the LZ GC B cell at 0, 10, and 15 min after BCR stimulation. We drew a radial line in each cell and analyzed the intensity over the length of that line for each time point. To quantify the membrane movement, we also inverted the grayscale IRM signal in each image in order to positively correlate the proximity to the coverslip with the intensity values above the background. After background subtraction, we calculated the change of mean fluorescence intensity of each cell. To count the contact sites of each cell, we ran another MATLAB algorithm that fits the image spots with modified Gaussian models. These modifications serve the purpose

of being able to recognize spots that aren't necessarily in the form of a PSF and captures more irregular shapes as long as they are a single 'spot.'

Detection and tracking of pod-like structures

For time-lapse live cell imaging, Igκ$^+$ naïve and LZ GC B cells were placed on PLB presenting anti-human Igκ or anti- rat Igκ antibodies surrogate antigens and incubated at 37°C on a climate-controlled stage with 5% CO_2 and 75% humidity, and DIC and IRM images were acquired at 3 sec intervals for 20 min. Movement of pod-like structures at early time point was measured for 3 min 45 sec from 2 min after activation and at late time point was measured for 8 min 45 sec from 11 min after activation on antigen-containing PLB. Analyses of time-lapse acquisitions were performed with MatLab and ImageJ. Pod-like structures from 3 LZ GC B cells exposed to high- or low-affnity antigen were analyzed and results were combined. First, any variations in intensity in DIC image sequences were normalized using linear regression in MatLab. Next, images were sharpened using an unsharp masking algorithm in MatLab to enhance the contrast of the pod-like structures. Pixels were next proportionately scaled down and binned into 8-bit unsigned integers to reduce the effects of small variations in pixel intensities. Masks were then created using a method similar to topographic prominence in ImageJ by iteratively applying the Maximum function to identify the local intensity maximum of pod-like structures as a single point. Points were then tracked over time and their diffusion coefficients calculated using Matlab code developed to track single particles as described previously (*38*).

Measurement and analysis of pulling forces

Antigen conjugated force and control sensors were produced and measurement of sensor opening was conducted as described previously (*26*). In our system, goat F(ab')$_2$ anti-human Igκ

(SouthernBiotech) and anti-human Igλ (SouthernBiotech) were used as surrogate antigen. For the movies, images were background subtracted and flatfield corrected in ImageJ (NIH) and value 1000 was added to Atto550 images before ratio calculation to reduce background. For the statistical analysis, images were acquired after 20 min of incubation of the cells in antigen-containing PLB, background subtracted and flatfield corrected in ImageJ. Using the threshold function, the ratio of Atto647N to Atto550 fluorescence in antigen clusters of each cell was calculated by ImageJ and statistical analysis of sensor opening from each B cell subset was calculated by Prism software (Graphpad).

Antigen extraction and trafficking

To measure antigen extraction, PMSs were prepared as described previously (*26*). Briefly, HEK293 cells were seeded onto poly-L-lysine coated chambers and cultured overnight in DMEM-10. Cells were washed and sonicated with a small probe at room temperature until their upper cell plasma membranes were removed. Sheared cells were then blocked in HBSS with 5% BSA and 2.5mM $CaCl_2$ at room temperature for 30 min, washed in a washing buffer of HBSS with 0.1% BSA, and incubated in washing buffer containing 50nM annexin V biotin (Biolegend). Cells were then washed, incubated in washing buffer containing 5ug/ml streptavidin (Sigma) for 30 min, washed, incubated in washing buffer containing either DyLight 550 (Innova Biosciences) conjugated anti-human Igκ antigen (GeneTex) or DyLight 550 (Innova Biosciences) conjugated anti-rat Igκ (ThermoFisher) surrogate antigen for 30 min, and washed again. Human tonsillar B cells were placed on PMSs and incubated at 37°C for 2 h. After incubation cells were harvested and stained with near-IR Live/Dead marker (ThermoFisher), DyLight 405 (Innova Biosciences) conjugated anti-IgD Fab (SouthernBiotech), BV786 anti-

CD10 (BD Biosciences), and the amount of signal was quantified by flow cytometry (BD LSR II).

To measure antigen trafficking, PMSs were prepared in the same manner as in the antigen extraction experiment and additional pHrodo avidin (ThermoFisher) was added. Briefly, cells were incubated in washing buffer containing annexin V biotin, streptavidin, and biotin- and DyLight 650-conjugated goat $F(ab')_2$ anti-human Igκ (Southern Biotech) and goat $F(ab')_2$ anti-human Igλ (Southern Biotech) sequentially with washing steps after every incubation. They were then incubated in washing buffer with pHrodo avidin for 30 min and washed in washing buffer. Cells were placed on PMSs and incubated either at 37°C or on ice for the times indicated in the figure legends. For the control, irrelevant antigen pc-BSA labeled with biotin and Alexa Fluor 647 was used instead of antigen. After incubation, cells were harvested, stained with near-IR Live/Dead marker (ThermoFisher), DyLight 405 (Innova Biosciences) conjugated anti-IgD Fab (SouthernBiotech), BV786 anti-CD10 (BD Biosciences), and the amount of signal was quantified by flow cytometry (BD LSR II).

Activation of naïve and LZ GC B Cells and measurement of IRF-4 mRNA expression

To activate LZ GC B cells, PLBs were prepared as described previously (*50*). Sorted $Ig\kappa^+$ naïve and LZ GC B cells were placed on PLB presenting anti-human Igκ, anti- rat Igκ antibodies surrogate antigens or without antigen and incubated at 37°C on a climate-controlled stage with 5% CO_2 and 75% humidity for 1 h. Then the same volume of RPMI-10 culture media containing anti-CD40 antibody (2ug/mL, R&D systems), IL-4 (40ng/mL, R&D systems), IL-21 (2ug/mL Biolegend), or RPMI-10 culture media alone was added to LZ GC B cells, and cells were incubated at 37°C for an additional 2 h and harvested. LZ GC B cells were lysed, RNA was

reverse transcribed, and cDNA was used to run TaqMan Gene Expression Assays using TaqMan Gene Expression Cells-to-C_T kit (ThermoFisher) on CFX connect Real-Time PCR Detection System (Bio Rad, check model name again). TaqMan Gene Expression Assays detecting IRF-4 (Hs00180031_m1, ThermoFisher) and ACTB (Hs1060665_g1, ThermoFisher) were used to measure levels of mRNA and ACTB was used for normalization. Data were analyzed by Prism software (GraphPad).

Measurement and analysis of surface molecule expression

Purified tonsillar B cells from three different individuals were either incubated in RPMI-10 at 37°C for 2 h or incubated in RPMI-10 containing 10ug/ml of goat $F(ab')_2$ anti-human Igκ (SouthernBiotech) and anti-human Igλ (SouthernBiotech) and 5ug/mL of streptavidin (Sigma) at 37°C for 2 to establish a resting population and activated population, respectively. Cells were then washed and stained with Live/Dead marker (ThermoFisher), anti-CD19 (Biolegend), anti-IgD (Miltenyi), anti-CD10 (BD Biosciences), and anti-CD184 (BD Biosciences). Each population was then barcoded to differentiate the individuals and activation states (*51*), washed, combined, and further stained for surface markers of interest with LEGENDScreen (Biolegend) human cell screening kit as per the manufacturer's protocol. After completing the staining, cells were washed and fixed, and fluorescent signals were quantified by flow cytometry (BD LSR II). Flow cytometry data was analyzed with FlowJo v.10.1 and Microsoft Excel 2016. First, each of the six barcoded populations corresponding to the three individuals and two activation states were gated into $CD10^-$ IgD^+ Naïve, $CD10^-$ IgD^- Memory, and $CD10^+$ IgD^- GC B cell subsets. GC B cells were further separated into $CD10^+$ IgD^- $CXCR4^{high}$ Dark Zone and $CD10^+$ IgD^- $CXCR4^{low}$ Light Zone subsets. Geometric means for the surface markers of interest were

calculated. To remove background due to unspecific binding, isotype readings from corresponding individuals with matching activation states were subtracted from barcoded populations for which staining antibodies of identical species and class had been used. To ensure the validity of the following calculations, a floor was set to adjust background-corrected values that were negative or very small. The naïve B cell subset was used as a control with which we compared the other subsets, and a threshold requirement was set based on the absolute difference between the naïve background-corrected values and the background-corrected values of their other corresponding subsets to filter out false positives arising from small variations at low fluorescence intensities. The fold changes over naïve were then calculated for each subset and displayed as the binary logarithm transformations of these ratios.

Acknowledgements

This work was supported by the Intramural Research Program of the National Institute of Health, National Institute of Allergy and Infectious Diseases. Authors would like to thank DC-CFAR Basic Science Core and Children's National Medical Center (CNMC) for providing tonsil specimens.

Author Contributions

K.K. and S.K.P. conceived and designed the study. K.K., N.Q., H.S., A.S., P.H., and J.L., performed experiments. K.K., N.Q., H.S., A.S., J.M., J.L., H.X., and C.X. analysed data. K.M.S., P.T. prepared DNA force sensor. K.K. wrote the original manuscript. N.Q., H.S., and S.K.P. edited the original manuscript. S.K.P. let the study.

Declaration of Interests

The authors declare no competing interests.

Figure legends

Figure 1. GC B Cells Engage Antigen through BCRs Concentrated in F-Actin and Ezrin-Rich Pod-like Structures. **(A)** DIC, IRM, and merged images of immune synapse of live naïve B cells placed on antigen-containing PLB and live LZ GC B cells placed on antigen-containing PLB or PLB with no antigen. **(B)** Kymographs of DIC images of naïve and LZ GC B cell immune synapse on antigen-containing PLB. **(C)** Membrane movement in the immune synapses of live naïve, LZ GC, and DZ GC B cells with time on antigen-containing PLB imaged by IRM. **(D)** STED super-resolution images of F-actin formed in immune synapses of naïve B cells and GC B cells placed on PLB that contained antigen. **(E)** Colocalization of F-actin and BCR in immune synapses of naïve and LZ GC B cells imaged by confocal microscopy on PLB that contained antigen. **(F)** (Left panel) Confocal microscopy images of immune synapses of naïve B cells and LZ GC B cells on antigen-coated PLB stained with Alexa Fluor 488 phalloidin for F-actin (green) and antibodies specific for ezrin (red). (Top right panel) Quantification of the MFI of ezrin and (Bottom right panel) colocalization of ezrin with F-actin (bottom) in the immune synapse of confocal images. **(G)** Bottom and orthogonal views of F-actin (green) and BCR (red) in naïve and LZ GC B cells imaged by confocal microscopy on antigen-containing PLB. **(H)** Side and top views of naïve and LZ GC B cells imaged by SEM on PLB without or with antigen. **(I)** Colocalization of pod-like structures and antigens in immune synapse of LZ GC B cells imaged by TIRFM on antigen-containing PLB. Scale bars are 5μm. *ns*>0.05, *$P \leq 0.05$, **$P \leq 0.01$, ***$P \leq 0.001$, and ****$P \leq 0.0001$ (unpaired *t*-test). Data are representative of two experiments (F: mean and s.e.m.).

Figure 2. Human GC B Cells Signal in Response to and Exert Pulling Forces on Membrane Bound Antigens through Pod-like Structures. **(A)** Immune synapses of naïve B cells and GC B cells imaged by TIRFM on PLB containing $F(ab')_2$ anti-λ/κ. **(B)** MFI of pPI3K and pSHP-1 and colocalization of BCR with pPI3K or pSHP-1 in the contact area of naïve and GC B cells placed on antigen-containing PLBs for 7 or 25 min. **(C)** (Top panels) Atto 647N FI (red) and Atto 550 (green) merged images. (Bottom panels) Sensor opening ratio (the ratio of Atto 647N FI to Atto 550 FI). **(D)** Quantification of sensor opening control sensors. **(E)** Colocalization of sensor opening locations and contact sites to the membrane with time imaged by TIRFM and IRM. Scale bars are 5μm. *ns*>0.05, *P≤0.05, **P≤0.01, ***P≤0.001, and ****P≤0.0001 (unpaired *t*-test). Data are representative of two experiments. (B and D: mean and s.e.m.)

Figure 3. Human GC B Cells Have a High-Affinity Threshold for Antigen. Naïve and LZ GC B cells were placed on PLB that did not contain antigen (resting) or placed on PLB that contained either high-affinity or low-affinity anti-κ mAbs. **(A)** TIRFM images were obtained of cells stained for the BCR and pCD79A. **(B-C)** Quantification of the BCR (**B**) and pCD79A (**C**) in the contact area of the B cells with the PLB in TIRFM images. **(D-F)** Quantification of TIRF images of cells stained with pSyk (**D**), pBLNK (**E**) and pPLCγ2 (**F**) in the contact area with the PLB of naïve and LZ GC B cells activated by high and low-affinity antigen for 7 or 25 min. **(G)** DIC and IRM images of naïve and LZ GC B cells imaged by TIRFM on PLB containing either high-affinity or low-affinity anti-κ mAbs. The still images were taken between 3 to 12 min of the supplementary movie 6. **(H)** Kymographs of IRM images of naïve and LZ GC B cell immune synapse on low- or high-affinity antigen-containing PLB. Red arrow heads on low-affinity naïve B cell are extended membrane ruffles and on high-affinity LZ GC B cell are pod-like structures

established stable contacts to antigen-containing PLB. **(I)** Quantitative analysis of pod-like structure movement in DIC images (number of tracks: n= 347 for high affinity early, n=887 for high affinity late, n=241 for low affinity early, and n=432 for low affinity late). Scale bars are 5μm. *ns*>0.05, *$P \leq 0.05$, **$P \leq 0.01$, ***$P \leq 0.001$, and ****$P \leq 0.0001$ (unpaired *t*-test). Data are representative of two experiments. (B-F: mean and s.e.m.)

Figure 4. Extraction and Trafficking of Membrane Associated Antigen Distinguishes GC B cells. **(A)** Antigen extraction by naïve and GC B cells placed for 2 h on PMS that contained either high-affinity or low-affinity anti-κ mAbs. Antigen-positive B cell populations were quantified by flow cytometry. **(B)** Transport of extracted antigens in naïve and LZ GC B cells placed on antigen-containing PMS. F-actin (green) and antigen (red). **(C)** Distance of MTOC in naïve and LZ GC B cells to antigen-containing PMS. F-actin (green), gamma-tubulin (cyan), antigen (red). **(D)** Localization and quantification of SNX9 or SNX18 in naïve and LZ GC B cells 45 min after activation on antigen-containing PMS imaged by confocal microscopy. F-actin (green), SNX9 and SNX18 (cyan), and antigen (red). MFI of SNX9 and SNX18 per each z-stack from the cell bottom to the top (n=25 per group). **(E)** Localization of SNX9 or SNX18 with MTOC in naïve and LZ GC B cells 45 min after activation on antigen-containing PMS. Alpha-tubulin (green), SNX9 and SNX18 (cyan), and antigen (red). **(F)** Localization pattern of LAMP-1 in naïve and LZ GC B cells (left) 30 min after activation on antigen-containing PMS. 3D colocalization of antigen with LAMP-1 in naïve and LZ GC B cells (right). LAMP-1 (cyan) and antigen (red). **(G)** Trafficking of extracted antigens to acidic intracellular compartments in naïve and LZ GC B cells with time on antigen-containing PMS. **(H)** Percentage of antigen-positive and pHrodo intensities (bottom left) of naïve B cells and LZ GC B cells which are similar in their

antigen acquisition. *ns*>0.05, *$P \leq 0.05$, **$P \leq 0.01$, ***$P \leq 0.001$, and ****$P \leq 0.0001$ (unpaired *t*-test). Data are representative of two (B-F) or three experiments (A, G, and H). (A, C, D and F: mean and s.e.m.)

Figure 5. Human GC B Cells Express IRF-4 in Response to High-Affinity Antigen in Combination with Tfh Cell Help. **(A-B)** Relative mRNA expression level of IRF-4 in naïve (**A**) and LZ GC B (**B**) cells after activation with antigens on PLB and/or Tfh like stimuli composed of anti-CD40 mAb, IL-21, and IL-4. *ns*>0.05, *$P \leq 0.05$, **$P \leq 0.01$, ***$P \leq 0.001$, and ****$P \leq 0.0001$ (paired *t*-test). (A-B: mean and s.e.m.)

Figure 6. The Differential Expression of Key Surface Markers may Further Contribute to Affinity Discrimination by Human GC B Cells. **(A)** Heat map: comparisons of differential surface molecule expression **(B-C)** Surface levels of CD29, CD49d, and VLA-4 active epitope in naïve and LZ GC B cells. **(D)** Binding ability of naïve and LZ GC B cells to VCAM-1 coated beads. *ns*>0.05, *$P \leq 0.05$, **$P \leq 0.01$, ***$P \leq 0.001$, and ****$P \leq 0.0001$ (unpaired *t*-test). Data are from one of five individuals (B) or data are from representative of three experiments (D) (C-D: mean and s.e.m.)

Supplementary Materials

Supplementary Figure 1. FACS sorting gating strategy for naïve, memory, LZ GC, DZ GC B cells. To discriminate naïve, memory, and GC B cells, IgD and CD10 are plotted. To further discriminate LZ GC and DZ GC B cells from GC B cells, CXCR4 and SSC-A are plotted.

Supplementary Figure 2. Quantification of dynamic movement of unique pod-like structures formed in the immune synapse of LZ GC B cell and expression level of BCR and ezrin. **(A)** Surface expression of BCR on naïve B cells, MBCs, LZ GC B cells and DZ GC B cells measured by flow cytometry of B cells stained with fluorescent dye-conjugated anti-Igκ and anti-Igλ. **(B)** Surface expression of IgM, IgG, IgA BCRs on GC B cells, naïve B cells and MBCs as measured by anti-Igκ or anti-Igλ. **(C)** Proximity of cell membrane to PLB in the immune synapse as measured from the center to the periphery of the area of interaction after 0 min (blue), 5 min (red), or 10 min (yellow) of activation. **(D)** Membrane movement in immune synapses of B cell subsets with time measured by quantification of change in intensity. **(E)** Counts of cell membrane contact sites of B cell subsets with time. Analysis methods are described in materials and methods. **(F)** The quantification of expression of ezrin in naïve, LZ GC, and DZ GC B cells by flow cytometry. *ns*>0.05, *$P \leq 0.05$, **$P \leq 0.01$, ***$P \leq 0.001$, and ****$P \leq 0.0001$ (unpaired *t*-test). Data are representative of three (A-B) or two experiments (C-D). (E-F: mean and s.e.m.)

Supplementary Figure 3. Antigen-induced BCR signaling in naive B cells and GC B cells. **(A)** MFI of pSyk-1, pPLCγ2, pVav, pBtk, and pCbl in immune synapse of naïve and GC B cells. **(B)** Colocalization of BCR and pSyk-1, pPLCγ2, pVav, pBtk, or pCbl in immune synapse of naïve

and GC B cells. **(C)** Colocalization of BCR and CD19 on live B cells with time on antigen-containing PLB as measured by quantification of TIRFM images (n= 8 per group). **(D)** Colocalization of BCR and pPI3K, pSHP-1, pVav, or pCbl in immune synapse of naïve B cells, IgM GC B and IgG GC B cells. **(E)** The growth of BCR cluster with time for naïve and GC B cells expressed as MFI of BCR labeled with Alexa Fluor 647-Fab anti-IgM for naïve B cells or anti-IgG for GC B cells (top panel) or fold change in the MFI of BCR clusters (bottom panel), measured as detailed in Materials and Methods (n=12 per group). *ns*>0.05, *$P \leq 0.05$, **$P \leq 0.01$, ***$P \leq 0.001$, and ****$P \leq 0.0001$ (unpaired *t*-test). Data are representative of two experiments. (A-D: mean and s.e.m.)

Supplementary Figure 4. Design of Force sensor and detection of pod-like structures and detection of pod-like structures. **(A)** F(ab')2 anti-κ/λ as a surrogate antigen conjugated to a 9 pN DNA-based force sensor. **(B)** Detection of pod-like structures of LZ GC B cell placed on high-affinity antigen-containing PLB.

Supplementary Figure 5. Polarization of SNX9 and SNX18 in naïve and LZ GC B cells after activation on antigen-containing PMS. **(A-B)** Quantification of SNX9 (**A**) and SNX18 (**B**) by flow cytometry. **(C-D)** Total fluorescence intensity (TFI) of SNX9 (**C**) and SNX18 (**D**) per each z-stack from the cell bottom to the top (n=25 per group). **(E)** Localization of SNX9 or SNX18 with MTOC in naïve and LZ GC B cells 45 min after activation on antigen-containing PMS. **(F)** Overlaid images of naïve B cells and LZ GC B cells. Scale bars are 5μm. *ns*>0.05, *$P \leq 0.05$, **$P \leq 0.01$, ***$P \leq 0.001$, and ****$P \leq 0.0001$ (unpaired *t*-test). Data are representative of two experiments (E). (A-D: mean and s.e.m.)

Supplementary Figure 6. The Differential Expression of Key Surface Markers. **(A)** The cell surface expression level of CD53, 81, 1a, 267, HLA-A B C, and CD59 that are highly expressed on GC B cells. **(B)** The cell surface expression level of CD23, 32, 35, 21, 22, and 31 that are lowly expressed on GC B cells. (C) The surface expression level of total tested. Data are representative of three experiments (A and B).

Supplementary Figure 7. Surface expression of LFA-1 and specificity of VLA-4 binding. **(A-B)** Surface expression level of CD11a and CD18 in naïve and LZ GC B cells. **(C)** Binding of B cells to beads coated with VCAM-1 or Human IgG isotype 30 min after incubation. **(D)** Binding ability of naïve and GC B cells to beads coated with human IgG as a control. **(E)** Surface expression level of integrin molecules in naïve and LZ GC B cells. *ns*>0.05, *$P \leq 0.05$, **$P \leq 0.01$, ***$P \leq 0.001$, and ****$P \leq 0.0001$ (unpaired *t*-test). Data are representative of five independent experiments (A), three experiments (C-D), or three individuals (E). (B: mean and s.e.m.).

Supplementary Movie 1. Distinctive membrane dynamics in the immune synapse of live naïve and LZ GC B cells placed on antigen-containing PLB were visualized by DIC (top panels) and IRM (bottom panels). Time-lapse imaging of naïve B cell (left panels) and LZ GC B cell (center panels) immune synapses upon activation, and LZ GC B cell (right panels) immune synapse without antigen.

Supplementary Movie 2. The dynamics of membrane movement in the immune synapse upon activation were visualized by IRM. Time-lapse imaging of naïve B cell (top left), LZ GC B cell (bottom left), and DZ GC cell (bottom right) immune synapses upon activation on antigen-containing PLB was observed by IRM. The grayscale IRM signal in each image was inverted and colored by fire LUT in order to positively correlate the proximity to the coverslip with the intensity.

Supplementary Movie 3. Time-lapse imaging of CD19 and BCR in the immune synapse of naïve B cells and LZ GC B cells. Naïve B cells and LZ GC B cells were activated by surrogate antigens presented on PLB and BCR (left panels, red) and CD19 (light panels, green) in the immune synapse of naïve (top panels) and LZ GC B (bottom panels) cells were imaged by TIRF.

Supplementary Movie 4. Pulling forces in the immune synapse of live naïve and LZ GC B cells were monitored with time using DNA-based force sensors. The force-insensitive label Atto550 (green) and the force-sensitive label Atto647N (red) channels were merged (naïve: top left, LZ

GC: bottom left) and the ratio of Atto647N/Atto550 defining sensor opening was calculated and visualized (naïve: top right, LZ GC: bottom right).

Supplementary Movie 5. Colocalization of the cell contact sites and the locations of pulling force in LZ GC B cell. Signals from the force-insensitive label Atto550 (green) and the force-sensitive label Atto647N (red) were merged (top left), the ratio of Atto647N/Atto550 defining sensor opening was calculated and visualized (top right), The dynamics of membrane movement in the immune synapse were measured by IRM (bottom left), and sensor opening and IRM were merged (bottom right).

Supplementary Movie 6. The dynamics of membrane movement in the immune synapse of naïve and LZ GC B cell upon activation by high- or low-affinity antigen were visualized by DIC (top panels) and IRM (bottom panels). Time-lapse live cell imaging of naïve B cell immune synapses activated by high-affinity (first panels) or low-affinity antigen (second panels) and LZ GC B cell immune synapses activated by high-affinity (third panels) or low-affinity antigens (fourth panels).

Supplementary Movie 7. Motile LZ GC B cells were observed upon activation by low-affinity antigen. Time-lapse live DIC (left panel) and IRM (right panel) imaging of LZ GC B cell immune synapse activated by low-affinity antigen.

Supplementary Movie 8. Distinct antigen transport pattern shown in human LZ GC B cells on PMS presenting surrogate antigens as compared to naïve B cells. Naïve (left) and LZ GC B cells

(right) in 3D. Signals from DyLight633 conjugated goat F(ab')$_2$ anti-human Igκ and anti-human Igλ surrogate antigens (red) and F-actin (green) were acquired by confocal microscopy.

Supplementary Movie 9. Localization of MTOC with SNX9 or SNX18 after activation in naïve and LZ GC B cells. Naïve (SNX9: top left, and SNX18: bottom left) and LZ GC B cells (SNX9: top right, and SNX18: bottom right) in 3D. Signals from DyLight633 conjugated goat F(ab')$_2$ anti-human Igκ and anti-human Igλ surrogate antigens (red), SNX9 or SNX18 (cyan), and alpha-tubulin (green) were acquired by confocal microscopy.

Supplementary Movie 10. Localization of LAMP-1 after activation in naïve and LZ GC B cells. Naïve (left) and LZ GC B cells (right) in 3D. Signals from DyLight633 conjugated goat F(ab')$_2$ anti-human Igκ and anti-human Igλ surrogate antigens (red), F-actin (green), and LAMP-1 (cyan) were acquired by confocal microscopy.

Figure 1.

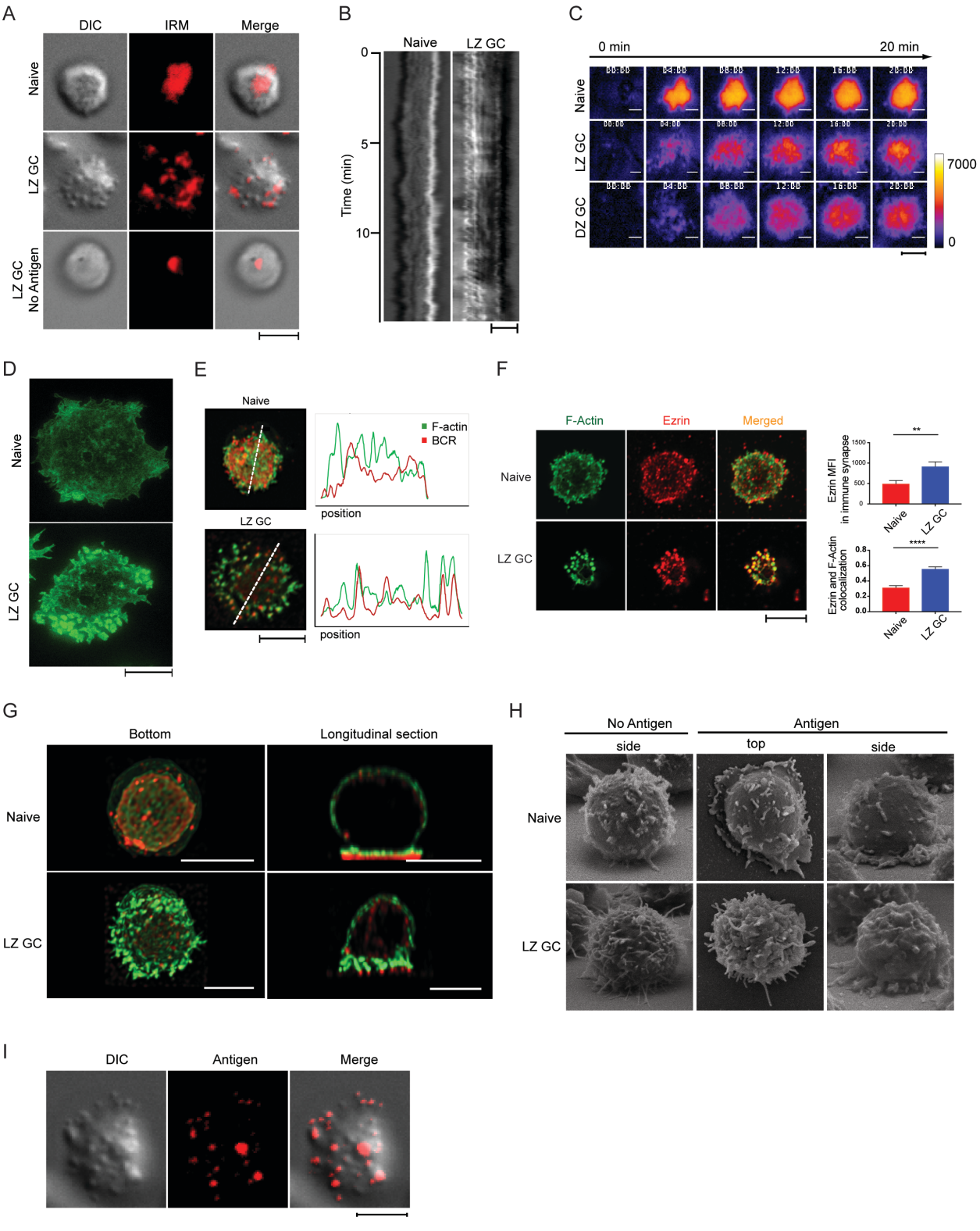
A
DIC
IRM
Merge
Naive
LZ GC
LZ GC
No Antigen
B
Naive
LZ GC
0
5
10
Time (min)
C
0 min
20 min
Naive
LZ GC
DZ GC
7000
0
D
Naive
LZ GC
E
Naive
LZ GC
F-actin
BCR
position
position
F
F-Actin
Ezrin
Merged
Naive
LZ GC
Ezrin MFI in immune synapse
Ezrin and F-Actin colocalization
Naive
LZ GC
G
Bottom
Longitudinal section
Naive
LZ GC
H
No Antigen
Antigen
side
top
side
Naive
LZ GC
I
DIC
Antigen
Merge

Figure 2.

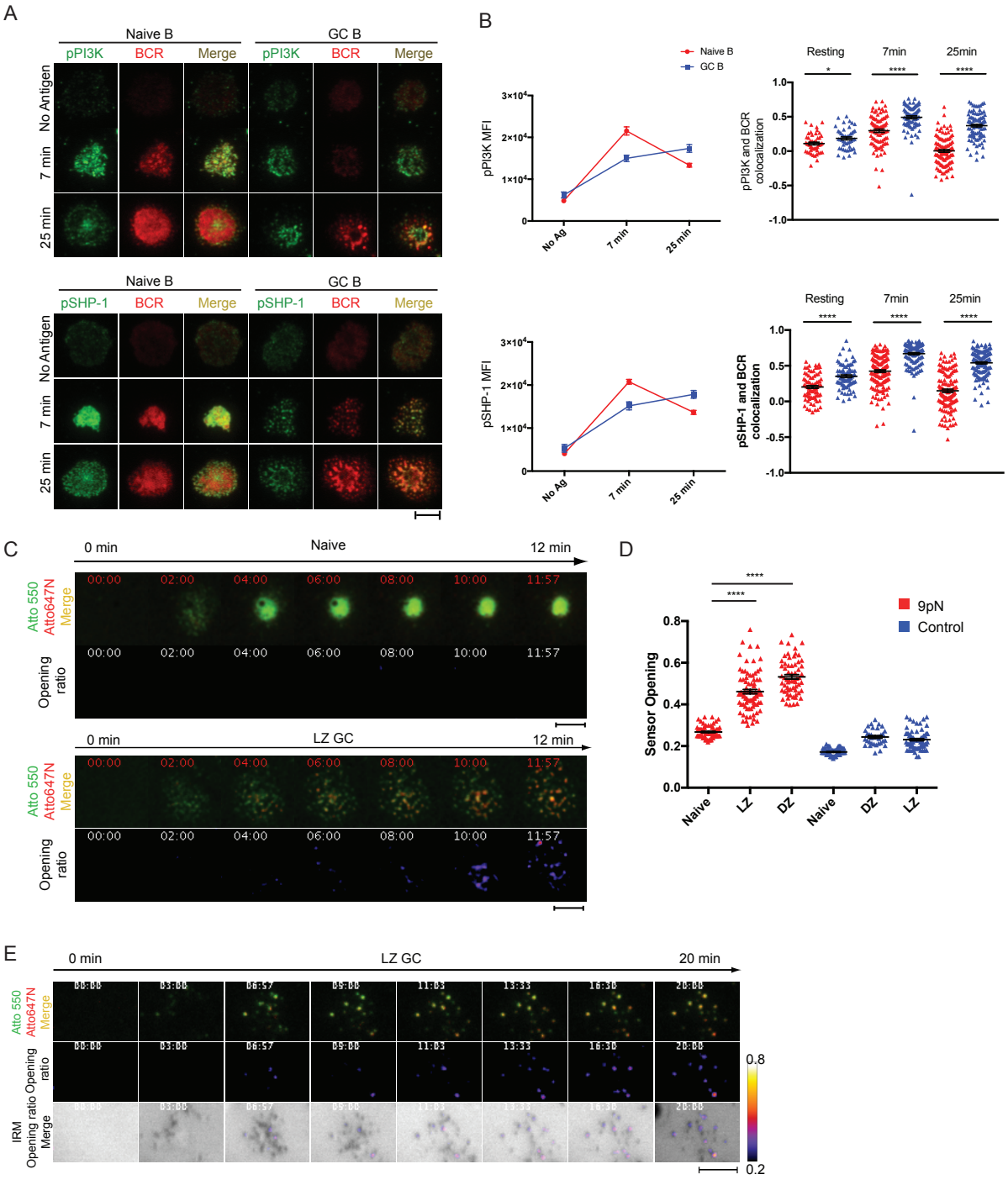
A
Naive B
GC B
pPI3K
BCR
Merge
No Antigen
7 min
25 min
pSHP-1
B
Naive B
GC B
pPI3K MFI
No Ag
7 min
25 min
Resting
7min
25min
pPI3K and BCR colocalization
pSHP-1 MFI
pSHP-1 and BCR colocalization
C
0 min
Naive
12 min
Atto 550
Atto647N
Merge
Opening ratio
LZ GC
D
9pN
Control
Sensor Opening
Naive
LZ
DZ
E
0 min
LZ GC
20 min
IRM
Opening ratio
0.8
0.2

Figure 3.

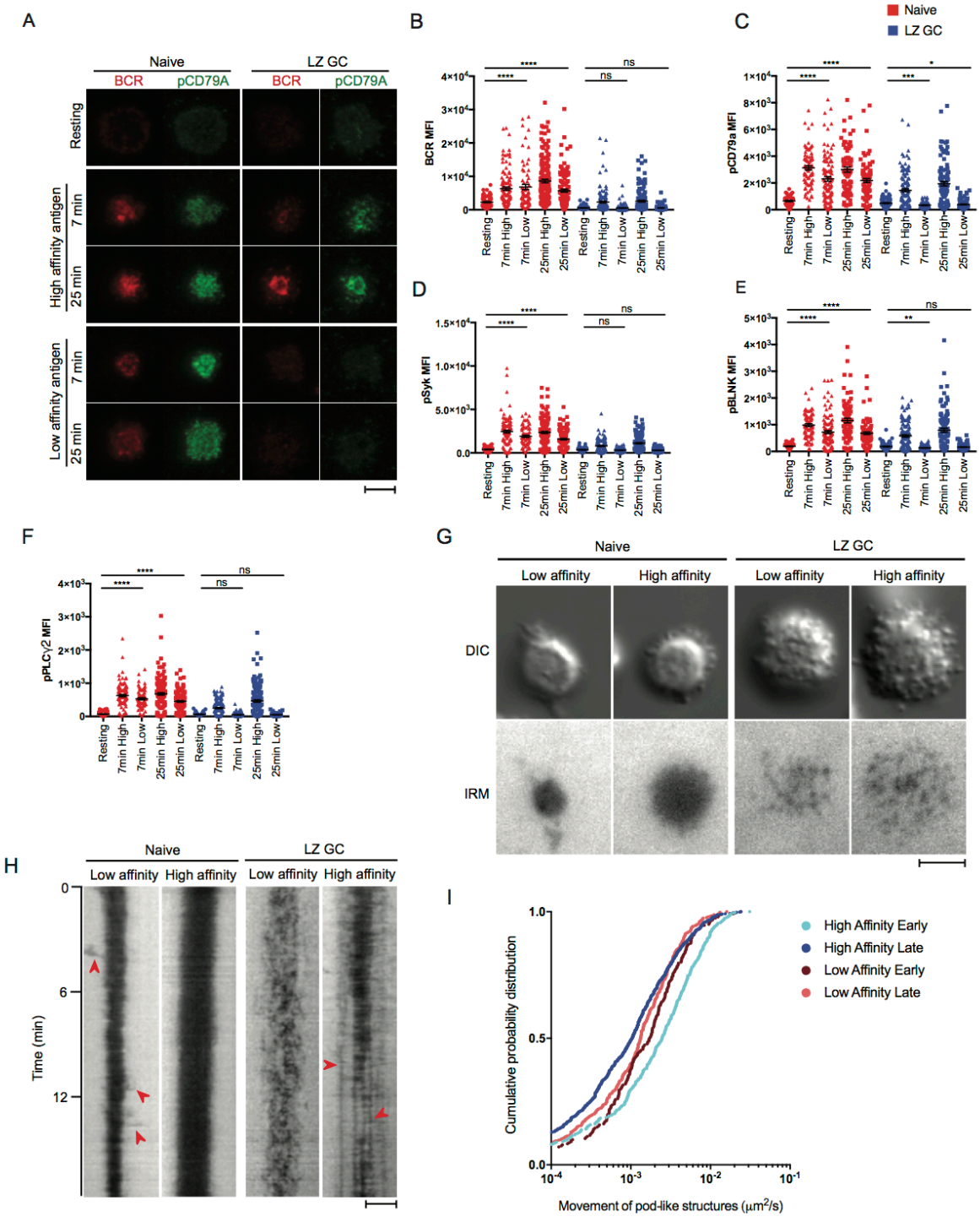
A
Naive
LZ GC
BCR
pCD79A
Resting
High affinity antigen
7 min
25 min
Low affinity antigen
B
BCR MFI
C
Naive
LZ GC
pCD79a MFI
D
pSyk MFI
E
pBLNK MFI
F
pPLCγ2 MFI
G
Low affinity
High affinity
DIC
IRM
H
Time (min)
I
Cumulative probability distribution
High Affinity Early
High Affinity Late
Low Affinity Early
Low Affinity Late
Movement of pod-like structures (μm²/s)

Figure 4.

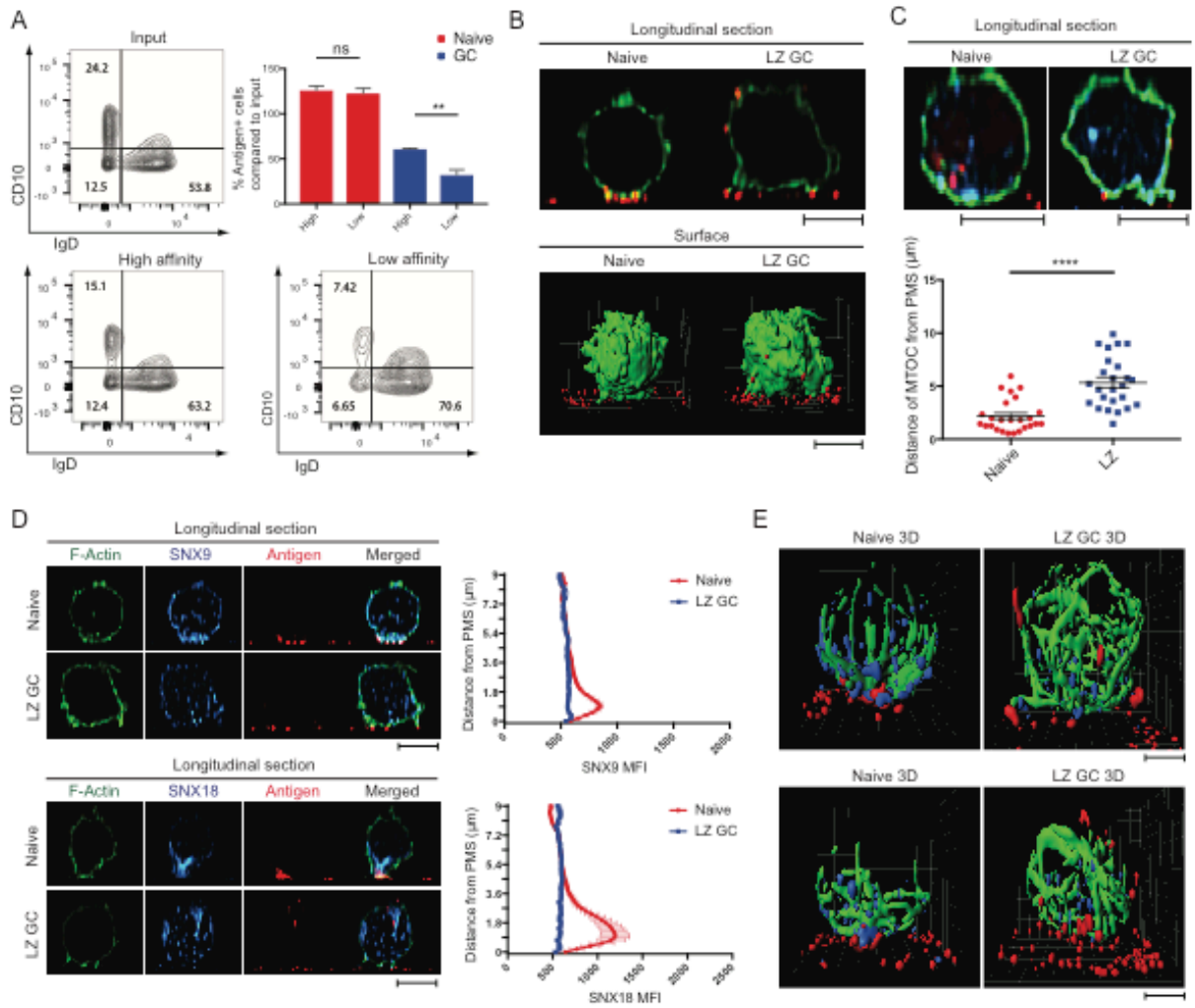
A
Input
CD10
IgD
24.2
12.5
53.8
ns
Naive
GC
% Antigen+ cells compared to input
High
Low
High affinity
15.1
12.4
63.2
Low affinity
7.42
6.65
70.6
B
Longitudinal section
Naive
LZ GC
Surface
C
Longitudinal section
Distance of MTOC from PMS (μm)
****
Naive
LZ
D
Longitudinal section
F-Actin
SNX9
Antigen
Merged
Naive
LZ GC
Distance from PMS (μm)
SNX9 MFI
SNX18
SNX18 MFI
E
Naive 3D
LZ GC 3D

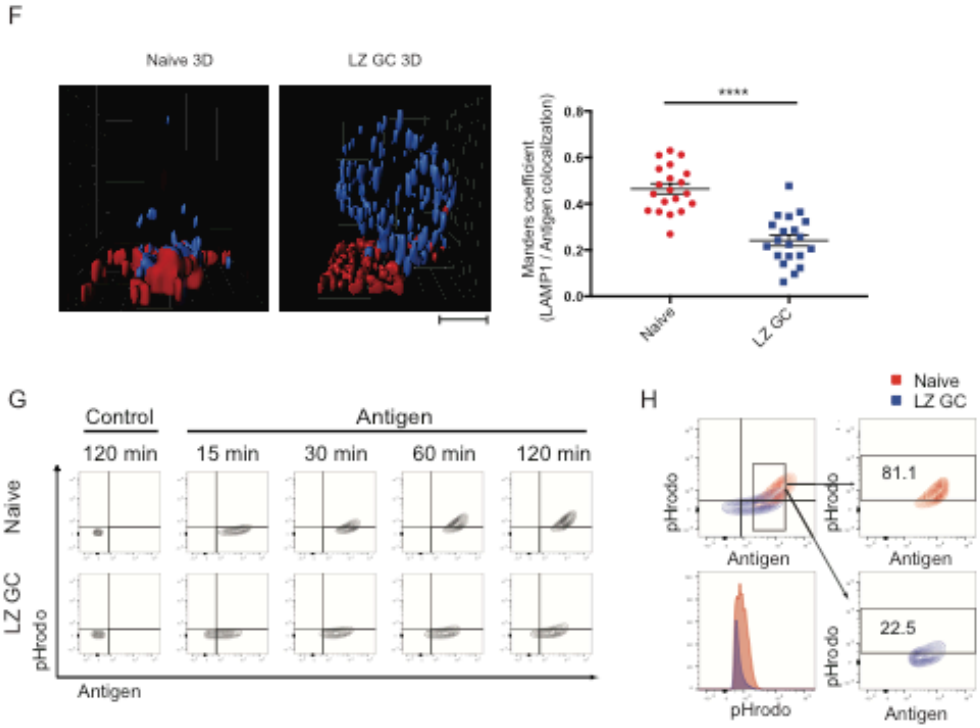
F
Naive 3D
LZ GC 3D
****
Manders coefficient
(LAMP1 / Antigen colocalization)
0.8
0.6
0.4
0.2
0.0
Naive
LZ GC
G
Control
Antigen
120 min
15 min
30 min
60 min
120 min
Naive
LZ GC
pHrodo
Antigen
H
Naive
LZ GC
pHrodo
Antigen
81.1
22.5

Figure 5.

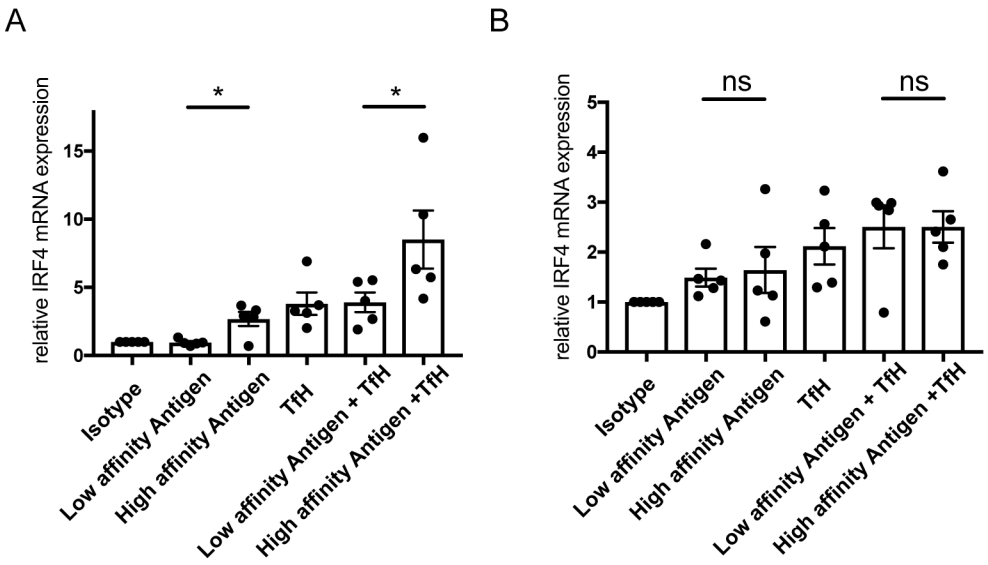
A
B
relative IRF4 mRNA expression
*
*
ns
ns
0
5
10
15
1
2
3
4
Isotype
Low affinity Antigen
High affinity Antigen
TfH
Low affinity Antigen + TfH
High affinity Antigen +TfH

Figure 6.

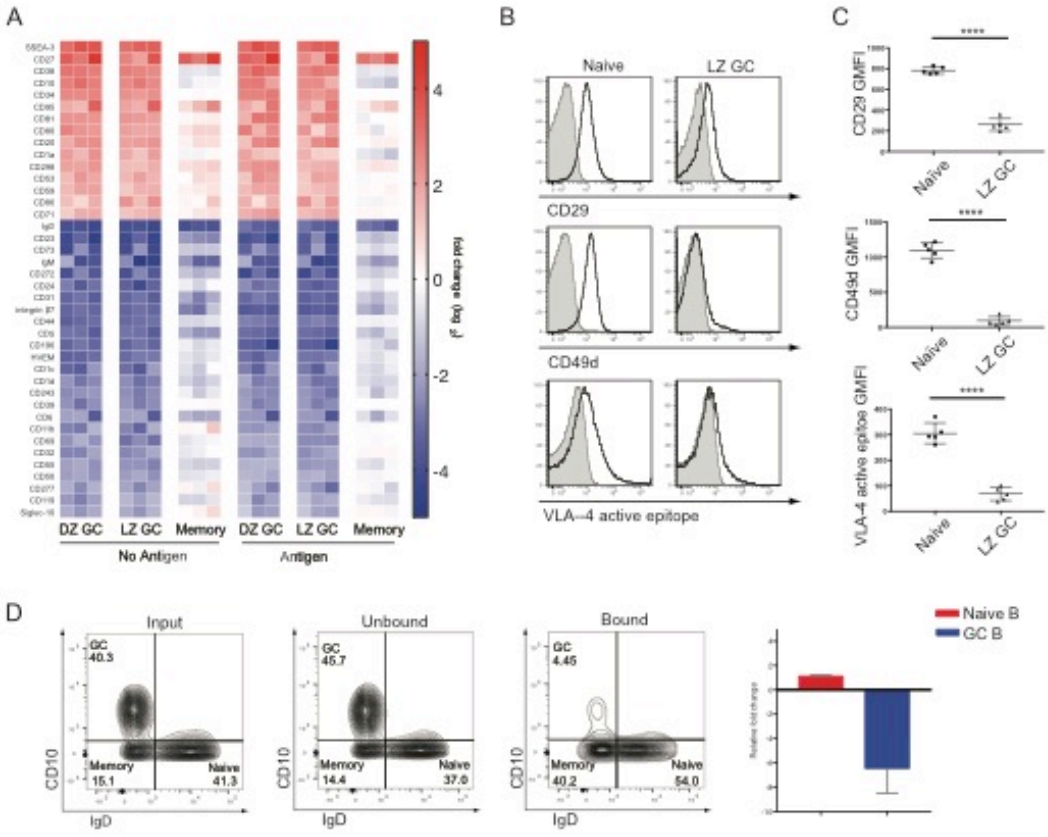
A
DZ GC
LZ GC
Memory
DZ GC
LZ GC
Memory
No Antigen
Antigen
4
2
0
-2
-4
B
Naive
LZ GC
CD29
CD49d
VLA–4 active epitope
C
CD29 GMFI
CD49d GMFI
VLA-4 active epitope GMFI
****
Naive
LZ GC
D
Input
Unbound
Bound
GC
40.3
45.7
4.45
Memory
15.1
14.4
40.2
Naive
41.3
37.0
54.0
CD10
IgD
Naive B
GC B

Supplementary Figure 1.

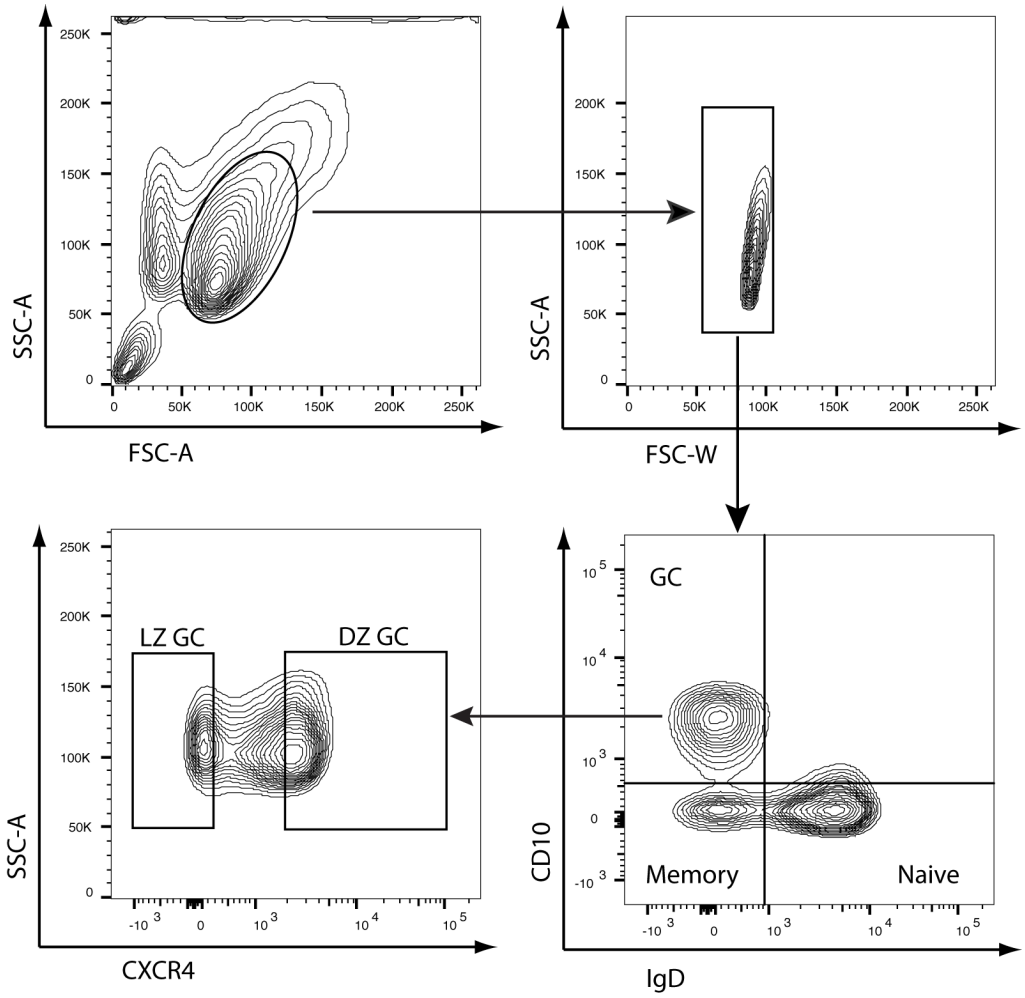

Supplementary Figure 2.

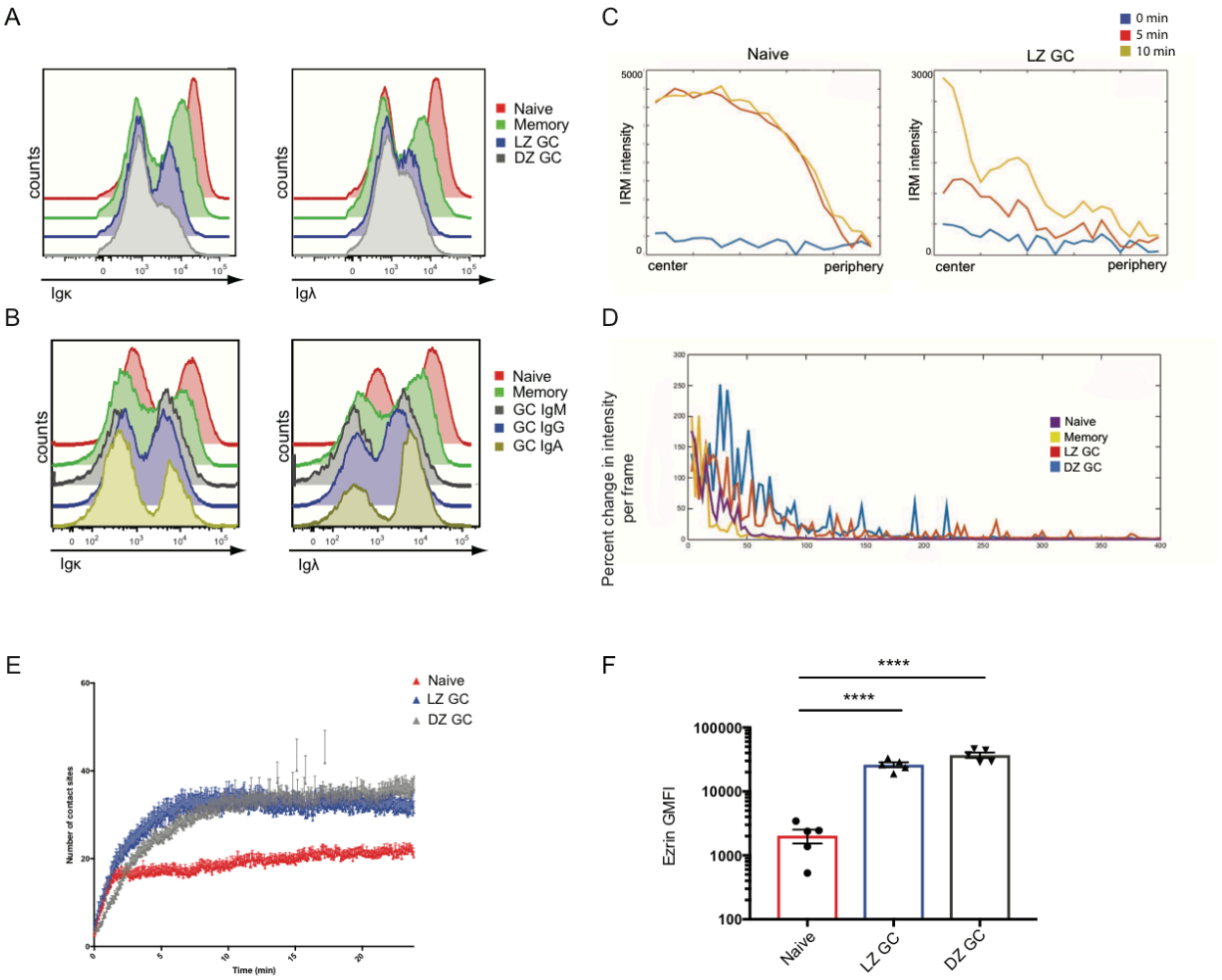

Supplementary Figure 3.

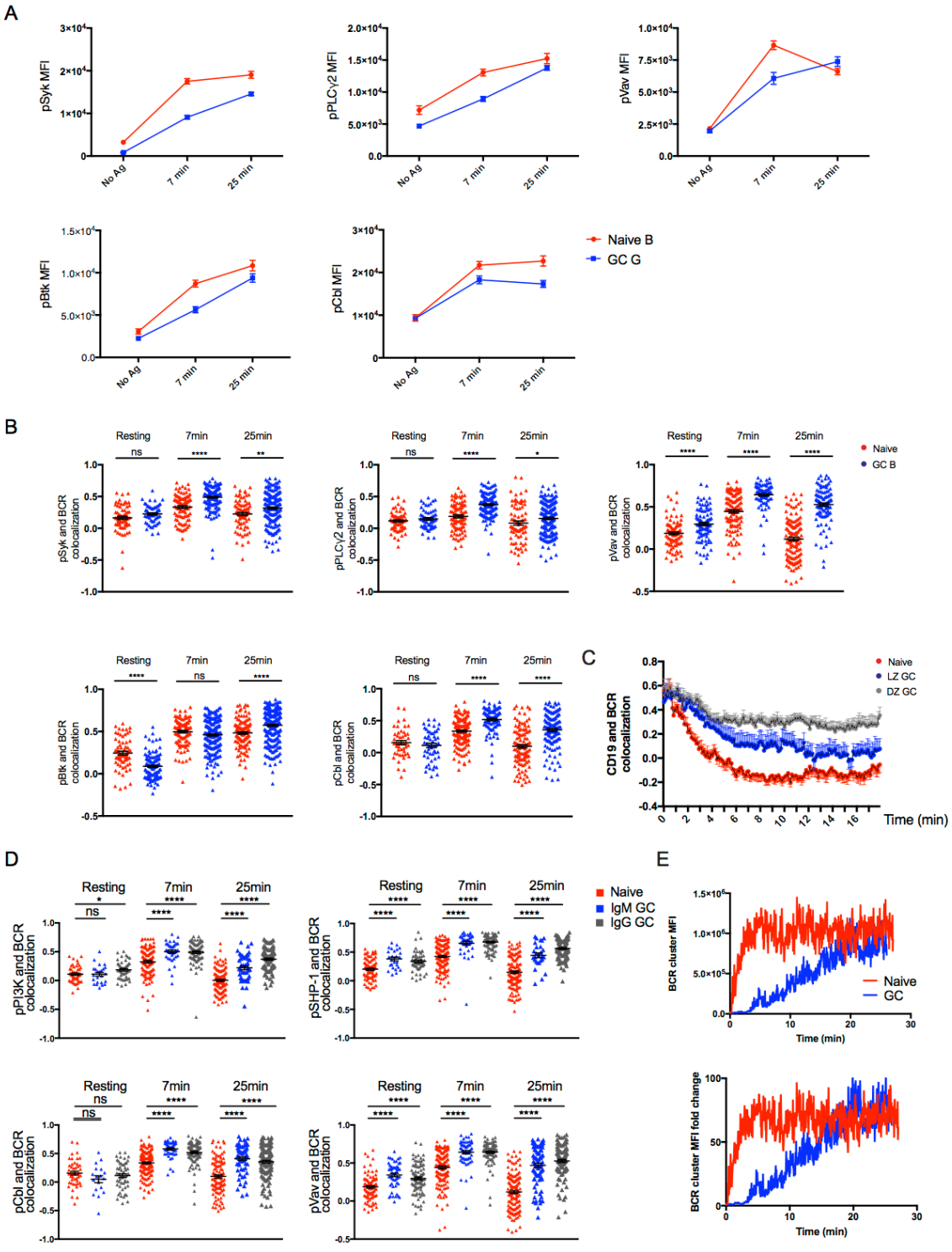

Supplementary Figure 4.

A

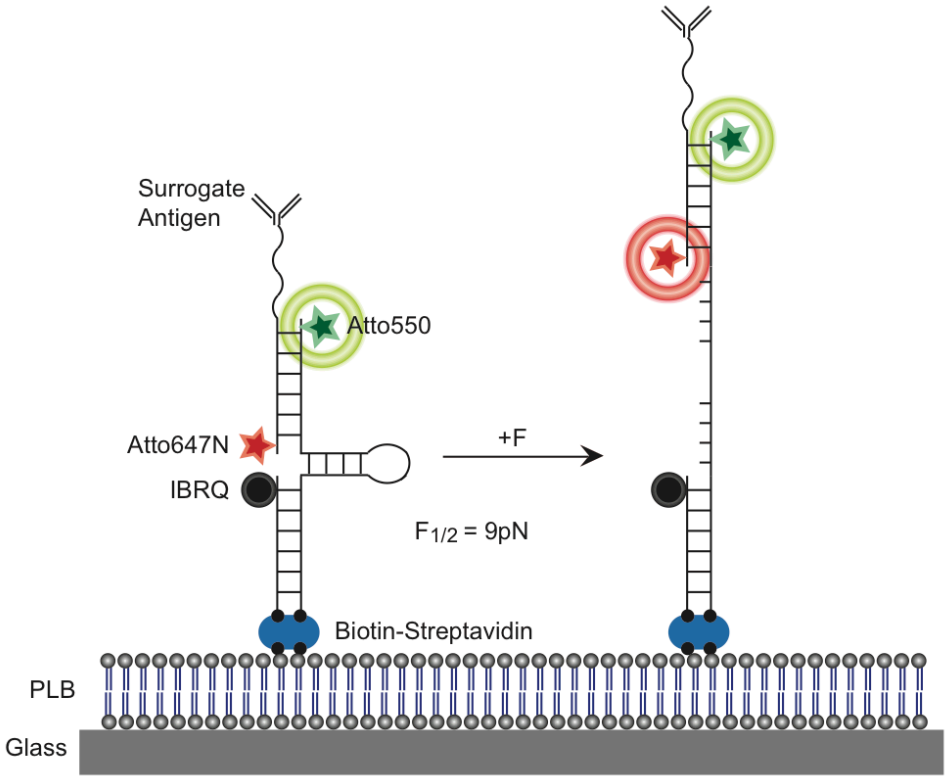

B

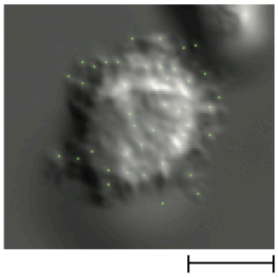

Supplementary Figure 5.

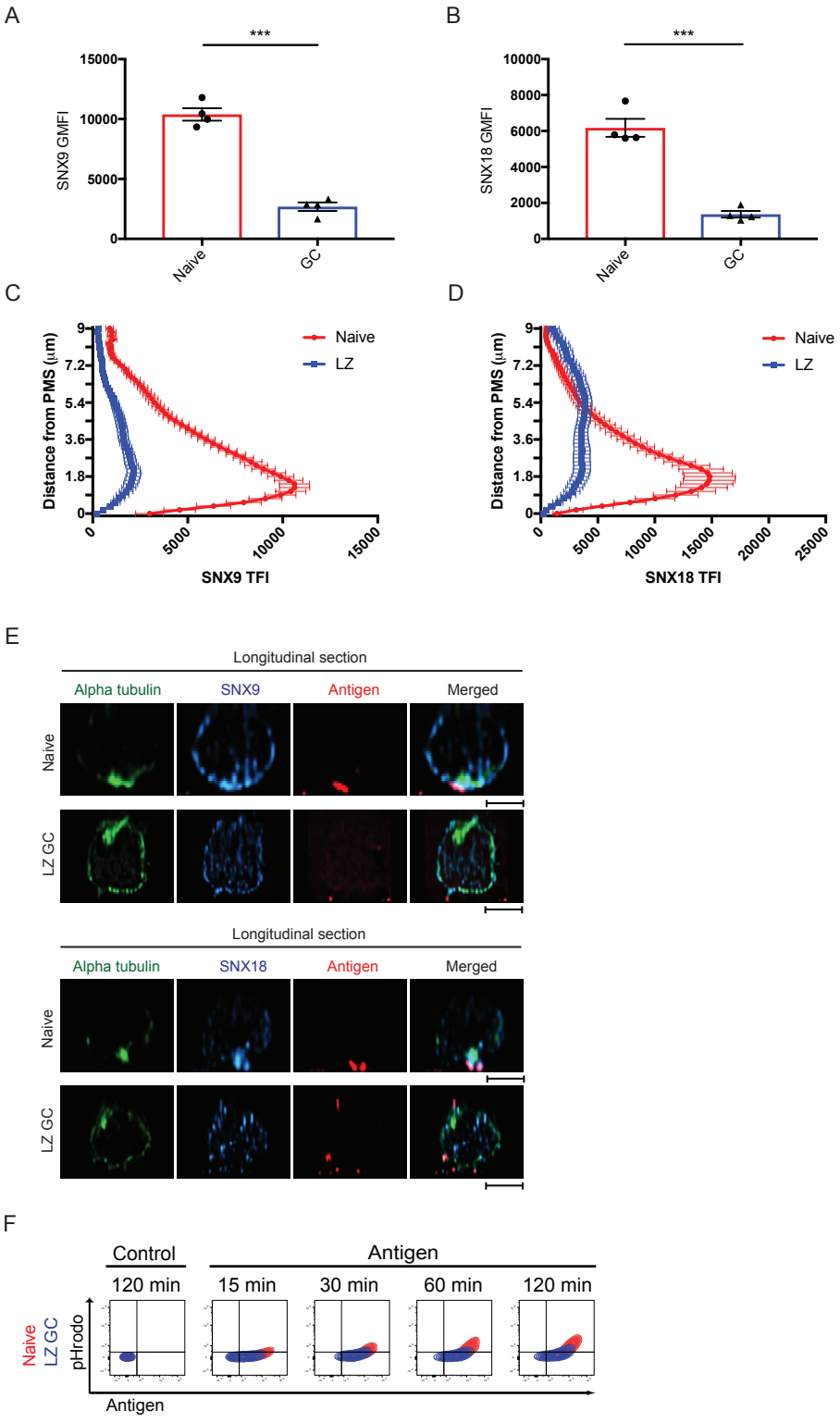

Supplementary Figure 6.

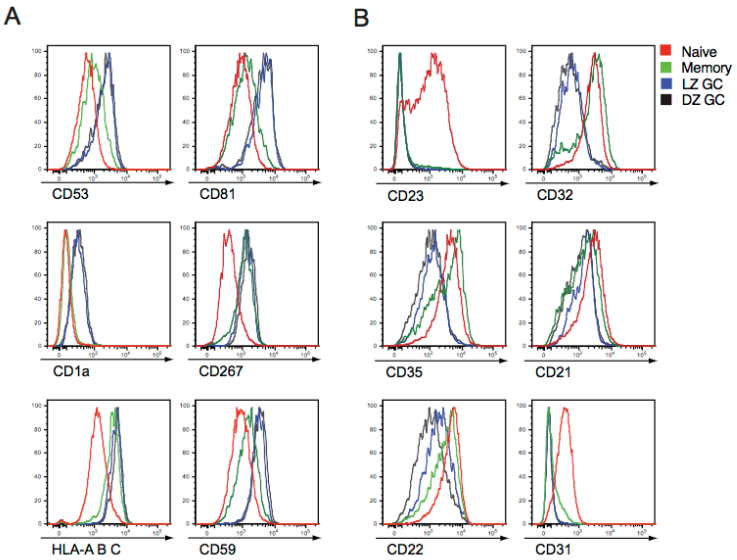

C

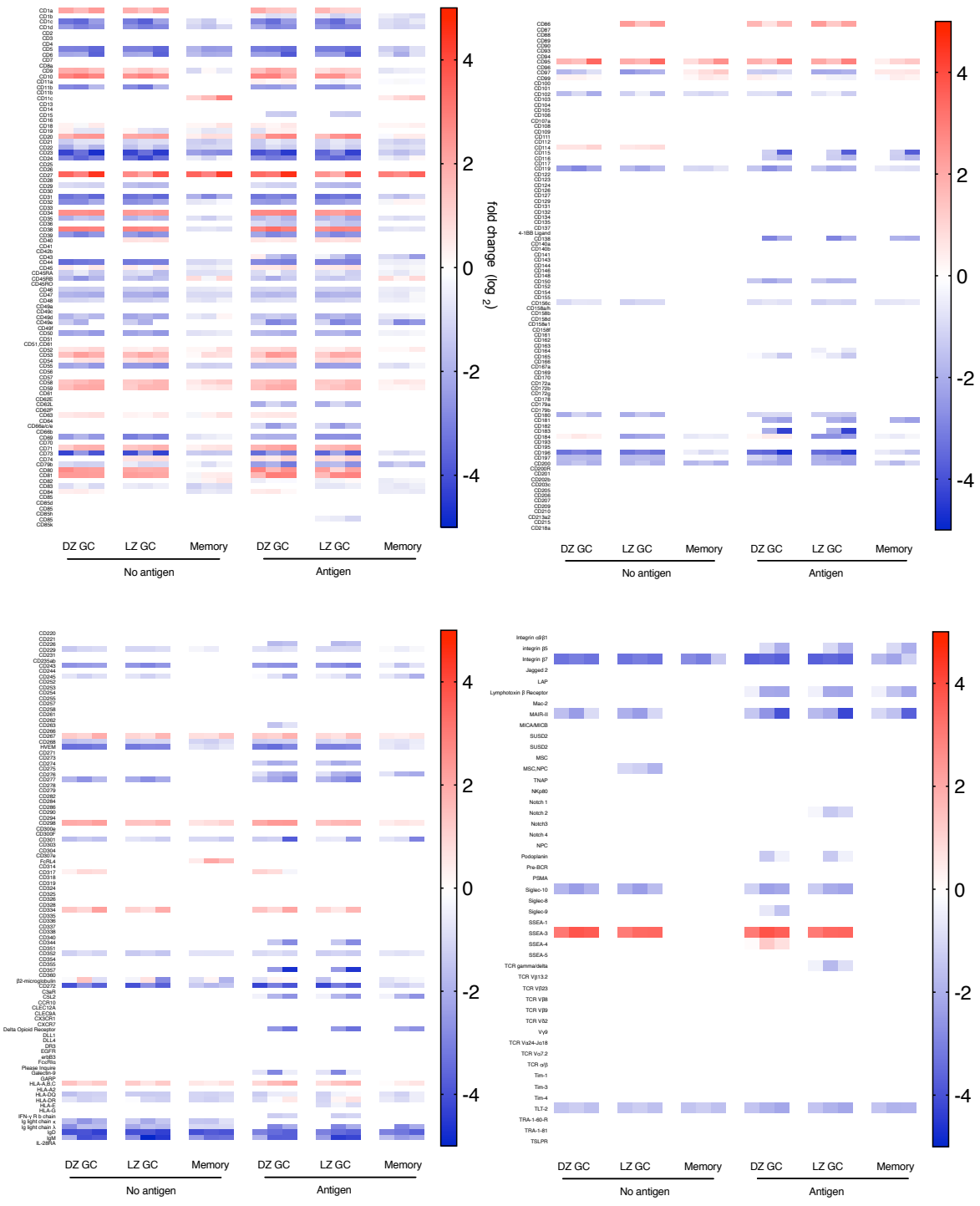
fold change (log 2)
4
2
0
-2
-4
DZ GC
LZ GC
Memory
DZ GC
LZ GC
Memory
No antigen
Antigen
DZ GC
LZ GC
Memory
DZ GC
LZ GC
Memory
No antigen
Antigen
DZ GC
LZ GC
Memory
DZ GC
LZ GC
Memory
No antigen
Antigen
DZ GC
LZ GC
Memory
DZ GC
LZ GC
Memory
No antigen
Antigen

Supplementary Figure 7.

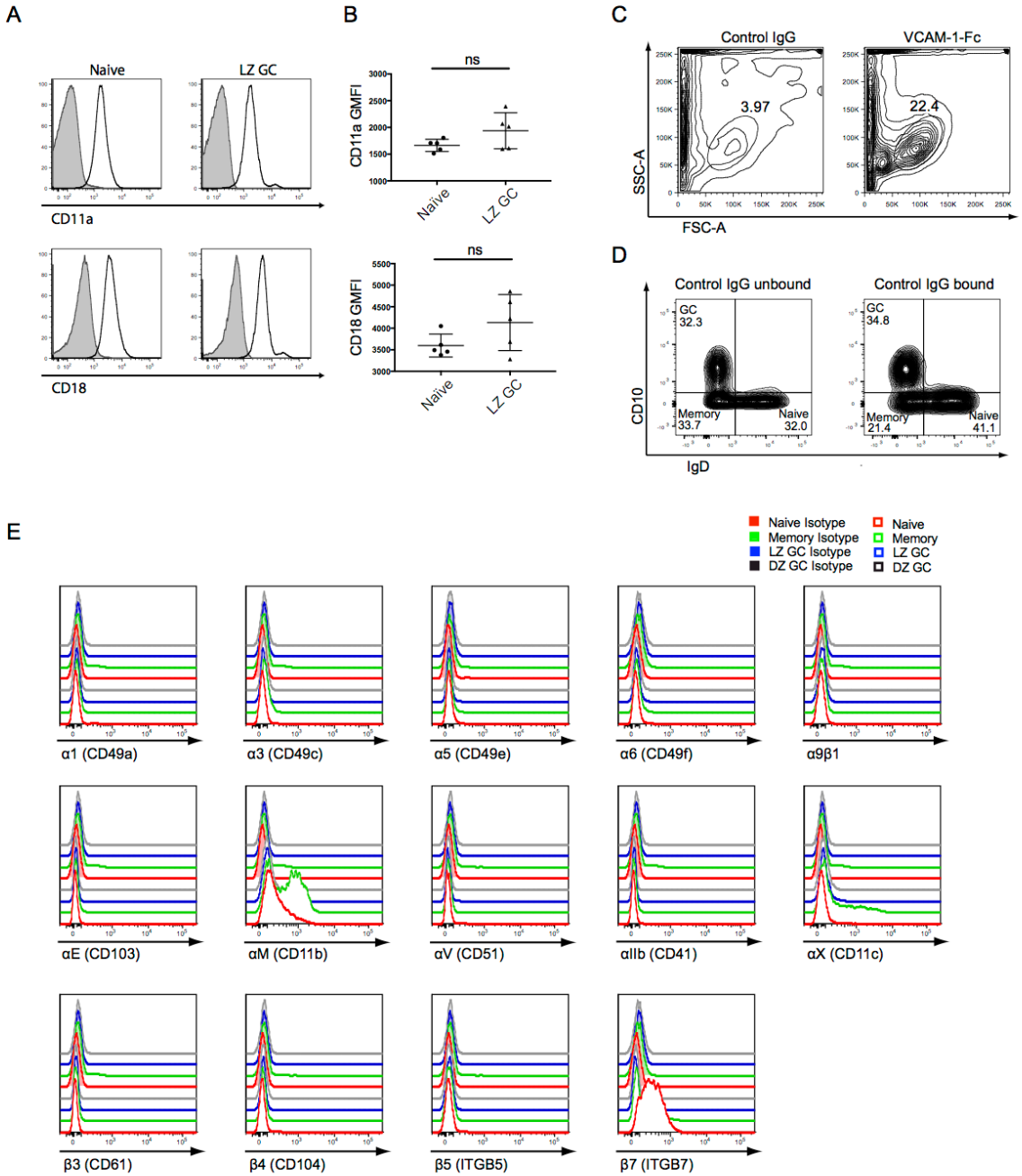

References

1. H. N. Eisen, G. W. Siskind, Variations in Affinities of Antibodies during the Immune Response. *Biochemistry* **3**, 996-1008 (1964).
2. N. S. De Silva, U. Klein, Dynamics of B cells in germinal centres. *Nat Rev Immunol* **15**, 137-148 (2015).
3. M. J. Shlomchik, F. Weisel, Germinal center selection and the development of memory B and plasma cells. *Immunol Rev* **247**, 52-63 (2012).
4. F. D. Batista, N. E. Harwood, The who, how and where of antigen presentation to B cells. *Nat Rev Immunol* **9**, 15-27 (2009).
5. R. Shinnakasu, T. Kurosaki, Regulation of memory B and plasma cell differentiation. *Curr Opin Immunol* **45**, 126-131 (2017).
6. L. Mesin, J. Ersching, G. D. Victora, Germinal Center B Cell Dynamics. *Immunity* **45**, 471-482 (2016).
7. O. Bannard, J. G. Cyster, Germinal centers: programmed for affinity maturation and antibody diversification. *Curr Opin Immunol* **45**, 21-30 (2017).
8. Y. R. Carrasco, F. D. Batista, B cells acquire particulate antigen in a macrophage-rich area at the boundary between the follicle and the subcapsular sinus of the lymph node. *Immunity* **27**, 160-171 (2007).
9. K. Suzuki, I. Grigorova, T. G. Phan, L. M. Kelly, J. G. Cyster, Visualizing B cell capture of cognate antigen from follicular dendritic cells. *J Exp Med* **206**, 1485-1493 (2009).
10. P. Tolar, Cytoskeletal control of B cell responses to antigens. *Nat Rev Immunol* **17**, 621-634 (2017).
11. T. Okada *et al.*, Antigen-engaged B cells undergo chemotaxis toward the T zone and form motile conjugates with helper T cells. *PLoS Biol* **3**, e150 (2005).
12. H. Qi, J. L. Cannons, F. Klauschen, P. L. Schwartzberg, R. N. Germain, SAP-controlled T-B cell interactions underlie germinal centre formation. *Nature* **455**, 764-769 (2008).
13. J. Jacob, G. Kelsoe, In situ studies of the primary immune response to (4-hydroxy-3-nitrophenyl)acetyl. II. A common clonal origin for periarteriolar lymphoid sheath-associated foci and germinal centers. *J Exp Med* **176**, 679-687 (1992).
14. J. J. Taylor, K. A. Pape, M. K. Jenkins, A germinal center-independent pathway generates unswitched memory B cells early in the primary response. *J Exp Med* **209**, 597-606 (2012).
15. J. M. Dal Porto, A. M. Haberman, G. Kelsoe, M. J. Shlomchik, Very low affinity B cells form germinal centers, become memory B cells, and participate in secondary immune responses when higher affinity competition is reduced. *J Exp Med* **195**, 1215-1221 (2002).
16. T. A. Shih, E. Meffre, M. Roederer, M. C. Nussenzweig, Role of BCR affinity in T cell dependent antibody responses in vivo. *Nat Immunol* **3**, 570-575 (2002).
17. T. A. Schwickert *et al.*, In vivo imaging of germinal centres reveals a dynamic open structure. *Nature* **446**, 83-87 (2007).
18. C. D. Allen, T. Okada, H. L. Tang, J. G. Cyster, Imaging of germinal center selection events during affinity maturation. *Science* **315**, 528-531 (2007).
19. A. E. Hauser *et al.*, Definition of germinal-center B cell migration in vivo reveals predominant intrazonal circulation patterns. *Immunity* **26**, 655-667 (2007).
20. G. D. Victora *et al.*, Germinal center dynamics revealed by multiphoton microscopy with a photoactivatable fluorescent reporter. *Cell* **143**, 592-605 (2010).
21. J. Wrammert *et al.*, Rapid cloning of high-affinity human monoclonal antibodies against influenza virus. *Nature* **453**, 667-671 (2008).

22. R. Shinnakasu *et al.*, Regulated selection of germinal-center cells into the memory B cell compartment. *Nat Immunol* **17**, 861-869 (2016).
23. N. J. Krautler *et al.*, Differentiation of germinal center B cells into plasma cells is initiated by high-affinity antigen and completed by Tfh cells. *J Exp Med* **214**, 1259-1267 (2017).
24. S. Malhotra, S. Kovats, W. Zhang, K. M. Coggeshall, B cell antigen receptor endocytosis and antigen presentation to T cells require Vav and dynamin. *J Biol Chem* **284**, 24088-24097 (2009).
25. E. Natkanski *et al.*, B cells use mechanical energy to discriminate antigen affinities. *Science* **340**, 1587-1590 (2013).
26. C. R. Nowosad, K. M. Spillane, P. Tolar, Germinal center B cells recognize antigen through a specialized immune synapse architecture. *Nat Immunol* **17**, 870-877 (2016).
27. E. Birgbauer, F. Solomon, A marginal band-associated protein has properties of both microtubule- and microfilament-associated proteins. *J Cell Biol* **109**, 1609-1620 (1989).
28. K. Goslin, E. Birgbauer, G. Banker, F. Solomon, The role of cytoskeleton in organizing growth cones: a microfilament-associated growth cone component depends upon microtubules for its localization. *J Cell Biol* **109**, 1621-1631 (1989).
29. R. Pakkanen, K. Hedman, O. Turunen, T. Wahlstrom, A. Vaheri, Microvillus-specific Mr 75,000 plasma membrane protein of human choriocarcinoma cells. *J Histochem Cytochem* **35**, 809-816 (1987).
30. N. Parameswaran, K. Matsui, N. Gupta, Conformational switching in ezrin regulates morphological and cytoskeletal changes required for B cell chemotaxis. *J Immunol* **186**, 4088-4097 (2011).
31. E. Cai *et al.*, Visualizing dynamic microvillar search and stabilization during ligand detection by T cells. *Science* **356**, (2017).
32. A. Stoddart, A. P. Jackson, F. M. Brodsky, Plasticity of B cell receptor internalization upon conditional depletion of clathrin. *Mol Biol Cell* **16**, 2339-2348 (2005).
33. F. Soulet, D. Yarar, M. Leonard, S. L. Schmid, SNX9 regulates dynamin assembly and is required for efficient clathrin-mediated endocytosis. *Mol Biol Cell* **16**, 2058-2067 (2005).
34. K. Haberg, R. Lundmark, S. R. Carlsson, SNX18 is an SNX9 paralog that acts as a membrane tubulator in AP-1-positive endosomal trafficking. *J Cell Sci* **121**, 1495-1505 (2008).
35. J. Park *et al.*, SNX18 shares a redundant role with SNX9 and modulates endocytic trafficking at the plasma membrane. *J Cell Sci* **123**, 1742-1750 (2010).
36. C. Watts, Antigen processing in the endocytic compartment. *Curr Opin Immunol* **13**, 26-31 (2001).
37. Y. R. Carrasco, F. D. Batista, B-cell activation by membrane-bound antigens is facilitated by the interaction of VLA-4 with VCAM-1. *Embo J* **25**, 889-899 (2006).
38. P. Tolar, J. Hanna, P. D. Krueger, S. K. Pierce, The constant region of the membrane immunoglobulin mediates B cell-receptor clustering and signaling in response to membrane antigens. *Immunity* **30**, 44-55 (2009).
39. V. Rolli *et al.*, Amplification of B cell antigen receptor signaling by a Syk/ITAM positive feedback loop. *Mol Cell* **10**, 1057-1069 (2002).
40. S. J. Fleire *et al.*, B cell ligand discrimination through a spreading and contraction response. *Science* **312**, 738-741 (2006).
41. L. F. Wang, C. E. Castro, M. C. Boyce, Growth strain-induced wrinkled membrane morphology of white blood cells. *Soft Matter* **7**, 11319-11324 (2011).
42. J. Wang *et al.*, Profiling the origin, dynamics, and function of traction force in B cell activation. *Sci Signal* **11**, (2018).
43. R. Lundmark, S. R. Carlsson, SNX9 - a prelude to vesicle release. *J Cell Sci* **122**, 5-11 (2009).

44. U. Klein *et al.*, Transcription factor IRF4 controls plasma cell differentiation and class-switch recombination. *Nat Immunol* **7**, 773-782 (2006).
45. R. Sciammas *et al.*, Graded expression of interferon regulatory factor-4 coordinates isotype switching with plasma cell differentiation. *Immunity* **25**, 225-236 (2006).
46. X. Li *et al.*, Cbl Ubiquitin Ligases Control B Cell Exit from the Germinal-Center Reaction. *Immunity* **48**, 530-541 e536 (2018).
47. S. L. Nutt, P. D. Hodgkin, D. M. Tarlinton, L. M. Corcoran, The generation of antibody-secreting plasma cells. *Nat Rev Immunol* **15**, 160-171 (2015).
48. X. Wang, L. B. Rodda, O. Bannard, J. G. Cyster, Integrin-mediated interactions between B cells and follicular dendritic cells influence germinal center B cell fitness. *J Immunol* **192**, 4601-4609 (2014).
49. Y. R. Carrasco, S. J. Fleire, T. Cameron, M. L. Dustin, F. D. Batista, LFA-1/ICAM-1 interaction lowers the threshold of B cell activation by facilitating B cell adhesion and synapse formation. *Immunity* **20**, 589-599 (2004).
50. W. Liu *et al.*, The scaffolding protein synapse-associated protein 97 is required for enhanced signaling through isotype-switched IgG memory B cell receptors. *Sci Signal* **5**, ra54 (2012).
51. B. Akkaya *et al.*, A Simple, Versatile Antibody-Based Barcoding Method for Flow Cytometry. *J Immunol* **197**, 2027-2038 (2016).